PERGAMON

International Journal of Solids and Structures 40 (2003) 7063–7092

INTERNATIONAL JOURNAL OF SOLIDS and STRUCTURES

www.elsevier.com/locate/ijsolstr

Localization and shear-crippling (kinkband) instability in a thick imperfect laminated composite ring under hydrostatic pressure ☆

Reaz A. Chaudhuri [a,*], Deokjoo Kim [b,1]

[a] *Department of Materials Science and Engineering, University of Utah, Salt Lake City, Utah 84112-0560, USA*
[b] *Department of Mechanical Engineering, University of Utah, Salt Lake City, Utah 84112-0560, USA*

Received 9 December 2002

Abstract

A fully nonlinear finite elements analysis for prediction of localization representing shear-crippling (kinkband) instability in a thick laminated composite (plane strain) ring (infinitely long cylindrical shell) under applied hydrostatic pressure is presented. The primary accomplishment of the present investigation is prediction of meso(lamina)-structure-related equilibrium paths, which are often unstable in the presence of local imperfections and/or material nonlinearity, and which are considered to "bifurcate" from the primary equilibrium paths, representing periodic buckling patterns pertaining to global or structural level stability of the thick cross-ply ring with modal or harmonic imperfection. The present nonlinear finite elements solution methodology, based on the total Lagrangian formulation, employs a quasi-three-dimensional hypothesis, known as layerwise linear displacement distribution theory (LLDT) to capture the three-dimensional interlaminar (especially, shear) deformation behavior, associated with the localized interlaminar shear-crippling failure.

A thick laminated composite [90/0/90] imperfect (plane strain) ring is investigated with the objective of analytically studying its premature compressive failure behavior. Numerical results suggest that interlaminar shear/normal deformation (especially, the former) is primarily responsible for the appearance of a limit (maximum pressure) point on the post-buckling equilibrium path associated with a periodic (modal or harmonic) buckling pattern, for which a modal imperfection serves as a perturbation. Localization of the buckling pattern results from "bifurcation" at or near this limit point, and can be viewed as a symmetry breaking phenomenon.

In order to investigate a localization of the buckling pattern, a local or dimple shaped imperfection superimposed on a fixed modal one is selected. With the increase of local imperfection amplitude, the limit load (hydrostatic pressure) decreases, and also the limit point appears at an increased normalized deflection. Additionally, the load–deflection curves tend to flatten (near-zero slope) to an undetermined lowest pressure level, signaling the onset of "phase transition" in the localized region, and coexistence of two "phases", i.e., a highly localized band of shear crippled (kinked)

☆ Dedicated to the occasion of 65th birthday of my dear friend and esteemed colleague, Professor George Dvorak of R.P.I.

* Corresponding author. Tel.: +1-801-581-6863; fax: +1-801-581-4816.
E-mail address: r.chaudhuri@m.cc.utah.edu (R.A. Chaudhuri).

[1] Presently at Agency for Defense Development, Taejon, Korea.

0020-7683/$ - see front matter
doi:10.1016/S0020-7683(03)00355-X

Nomenclature

$[A]$ diagonal matrix composed of Aitken acceleration factors

$[B_{\mathrm{LL}}^{(k)}]$ linear differential operator matrix relating the linear incremental strain components to incremental displacement components in the kth layer

$[B_{\mathrm{LN}}^{(k)}]$ linear differential operator matrix relating the linearized incremental strain components to incremental displacement components in the kth layer

$[B_{\mathrm{NN}}^{(k)}]$ linear differential operator matrix relating the nonlinear incremental strain components to incremental displacement components in the kth layer

b,t subscript or superscript indicating the bottom and the top surface, respectively

${}_0C_{\mathrm{ijrs}}$ incremental elastic stiffness (material property) tensor

c characteristic constant related to local imperfections

${}^{t+\Delta t}\mathrm{d}s$ differential loading surface area evaluated at the first iteration of each load step when hydrostatic pressure is applied

${}^0\mathrm{d}V$ infinitesimal control volume with respect to the initial configuration

E_{LL}, E_{TT},ν_{LT} longitudinal and transverse Young's moduli, and major Poisson's ratio, respectively, of a unidirectional lamina

${}_0\bar{e}_{ij}^{\mathrm{L}}$ linear incremental component of the 6×1 strain vector

${}_0\bar{e}_{ij}^{\mathrm{N}}$ linearized incremental component of the 6×1 strain vector

$\{f_{\mathrm{L}}\}$ applied load vector

${}^{t+\Delta t}\{f_{\mathrm{L}}\}$ applied load vector at the time $t+\Delta t$

$\{f_{\mathrm{N}}\}$ nonlinear internal force vector

${}^{t+\Delta t}\{f_{\mathrm{N}}\}^{(i)}$ nonlinear internal force vector at the ith iteration of the time step between t and $t+\Delta t$

G_{LT},G_{TT} longitudinal and transverse shear moduli, respectively

$g_k^{(i)}(z)$ coefficient of the first fundamental differential quadratic form of a parallel surface of the ith layer in the kth direction, $k=1(x),\ 2(\beta),\ 3(z)$

$\bar{g}_{\beta}^{(i)}$ coefficient of the first fundamental differential quadratic form of the bottom surface of the ith layer in the βth direction

h_{i},h thickness of the ith lamina and the laminated shell, respectively

$[K_{\mathrm{L}}]$ linear global stiffness matrix

$[K_{\mathrm{N}}]$ nonlinear contribution to the global geometric stiffness matrix

m ratio of reference yielding stress to transverse shear modulus in Ramberg–Osgood representation

N total number of elements

N_{L}, N_{S} number of elements for each layer and number of layers, respectively

$\mathbf{n}^{(k+1)}$ unit normal vector for the top surface of the kth layer with respect to the fixed coordinate system

$\{{}^{t+\Delta t}\mathbf{n}^{(N_{\mathrm{S}}+1)}\}$ normal direction vector of the loaded surface $(N_{\mathrm{S}}+1)$ evaluated at the first iteration of each load step when hydrostatic pressure is applied

P_{r} applied hydrostatic pressure

p uniform hydrostatic pressure

p_{cr} classical buckling pressure of a long cylinder

$[Q^{(k)}]$, $[\overline{Q}^{(k)}]$ incremental elastic stiffness (material property) matrix for the kth orthotropic and anisotropic layer, respectively

$Q_{ij}^{(k)}$, $\overline{Q}_{ij}^{(k)}$ incremental elastic stiffness matrix components of the kth orthotropic and anisotropic layer, respectively

$\{{}_0Q\}^{(i)}$ incremental displacement vector due to the applied load vector

R_{i} inner radius of a long perfect cylinder (plane strain ring)

${}^{t+\Delta t}\Re$ external virtual work done on a body

$\{{}_0R\}^{(i)}$ incremental displacement vector due to the residual force vector

$r_0(\theta)$, $R_0(\theta)$ radial coordinates of the innermost (bottom) surface of an undeformed and deformed ring, respectively, with modal imperfection

$r(\theta)$, $R(\theta)$ radial coordinates of the innermost (bottom) surface of an undeformed and deformed ring, respectively, with combined modal/local imperfection

${}^{t+\Delta t}S$ loading surface area evaluated at the first iteration of each load step when hydrostatic pressure is applied

${}_0S_{ij}^{(k)}$ incremental stress component of the kth layer

${}^{t+\Delta t}{}_0S_{ij}$ second Piola–Kirchhoff stress tensor at time $t+\Delta t$ evaluated with respect to the initial configuration

$[{}_0^t\widehat{S}_{ij}]$ 9×9 stress matrix evaluated at time t

$\{{}_0^t\overline{S}_{ij}\}$ 6×1 stress vector evaluated at time t

$\{{}^{t+\Delta t}{}_0\overline{S}^{(k)}\}^{(i-1)}$ element stress vector of the kth layer evaluated at the $(i-1)$th iteration of each load step

t time as an index

${}_0U_{\mathrm{bk}}^{(i)}$, ${}_0V_{\mathrm{bk}}^{(i)}$ incremental nodal displacement components at the kth node on the

${}_0W_{\mathrm{bk}}^{(i)}$ bottom surface of the ith layer in x^1(or x), x^2(or β), and z directions, respectively

${}_0U_{\mathrm{tk}}^{(i)}$, ${}_0V_{\mathrm{tk}}^{(i)}$ incremental nodal displacement components at the kth node on the top

${}_0W_{\mathrm{tk}}^{(i)}$ surface of the ith layer in x^1 (or x), x^2 (or β), and z directions, respectively

${}^{t+\Delta t}\{\mathbf{V}\}^{(i)}$ total displacement vector at the ith iteration of the time step between t and $t+\Delta t$

${}_0V_q$ the qth displacement prescribed at each time step for the displacement increment method

w_0,w_1 amplitudes of modal and local imperfections, respectively, of a ring

x,β,z coordinates of a point inside a layer

x^k global Cartesian coordinate coordinates, $k=1,2,3$

ε_{ij} physical component of the Green–Lagrange strain tensor

${}_0\varepsilon_{ij}^{(k)}$ incremental strain component of the kth layer

${}^{t+\Delta t}{}_0\varepsilon_{ij}$ total Green–Lagrangian strain tensor evaluated with respect to the initial configuration at time $t+\Delta t$

ε_{f},ε_{c} force and energy convergence criteria, respectively

$\hat{\eta}_{ki}$,$\delta\hat{\eta}_{ki}$ 9×1 nonlinear strain component vector and its variation, respectively

${}_0\lambda^{(i)}$ incremental load scale factor due to the prescribed displacement component

$[\Phi]$ quadratic global interpolation function matrix

θ angle measured from the global x^3 axis

$\rho^{(i)}$ radius of curvature of the inner surface of the ith layer of an imperfect cylindrical shell/ring

Σ_{ij} component of the incremental compliance matrix of a lamina

$\Psi_k(r,s)$ quadratic element interpolation function in terms of r and s

ζ radial distance of a point inside a laminated ring measured from its bottom surface

phase and its unshear-crippled (unkinked) counterpart along the circumference of the ring. Interlaminar shear-crippling triggered by the combined effect of imperfection, material nonlinearity and interlaminar shear/normal deformation appears to be the dominant compressive failure mode. A three-dimensional or quasi-three-dimensional theory, such as the afore-mentioned LLDT is essential in order to capture the meso-structure-related instability failure such as localization of the interlaminar shear crippling, triggered by the combined presence of local imperfection and material nonlinearity.

1. Introduction

Advanced laminated composite materials, e.g., carbon/epoxy, carbon/PEEK, etc., are increasingly being used in hydrospace applications. Pressure hulls of submersibles, such as those used in search and rescue operations, e.g., in the Russian submarine, Kursk, disaster, constitute one such example. Feasibility studies pertaining to the use of fiber-reinforced composite materials for deep submergence pressure applications have been carried out by the US Navy since 1960s (Couch et al., 1969). The composites used in such hydrospace applications must, by necessity, be thick-sections in order to avoid catastrophic collapse caused by global (structural) buckling, and must sustain large hydrostatic compressive loads. Their deformation and failure behavior (e.g., buckling/post-buckling, shear crippling, kinking, etc.) are of great concern to marine/submersible structural designers.

Garala (1989) has carried out extensive experimental and numerical evaluations of advanced (e.g., carbon/epoxy) composite thick unstiffened cylindrical shell specimens, e.g., inner radius to thickness ratio, $R_i/h \approx 6.0$, $R_i \approx 8.89$ cm (3.5 in.) and length, $L \approx 20.32$ cm (8.0 in.), subjected to external pressure loading (Fig. 1). He has reported details of (a) fabrication methods of cylinders, (b) experimental data on collapse pressures, strains and damage assessment, obtained using strain gages and acoustic emission (AE), and (c) structural analyses for prediction of stresses and collapse pressures, performed using standard finite element codes, e.g., ABACUS. The key observations can be summarized as follows: (a) the observed hoop stress level of approximately 579 MPa (84 ksi) is considerably lower than the estimated value of 1.1 GPa (160 ksi) based on thin-section composites experience (using the rule of mixtures with 1.655 GPa (240 ksi) insitu fiber strength); (b) unacceptably low failure external pressure in the 83 MPa (12 ksi) range has generally been observed with certain exceptions, as compared to the computed value of 152 MPa (22 ksi) based on the above estimated hoop stress value; (c) a considerable amount of scatter has been observed in the test data; and (d) fabrication defects are believed to have a detrimental effect on the compressive strength. Abdallah et al. (1990) have conducted a series of innovative tests on thick composite rings (Fig. 2) under external pressure, using an especially designed bladder and obtained extensive data by means of strain gages, AE, photoelasticity and Moiré interferometry. In general, although the ring specimens failed at pressures 10–25% higher than their cylindrical counterparts, made of the same material systems, almost identical failure mechanisms are observed in both sets of specimens.

Starnes and Williams (1982) have reported a shear crippling (kinkband) type of failure to be prevalent in 0°-plies of a 48-ply laminate in the immediate vicinity of a hole as well as in a localized region of low velocity impact damage prior to catastrophic failure under compression. It may be remarked that shear crippling and kinkband represent the same instability phenomenon viewed at two geometrical scales: the former at the meso-structural (lamina) level, while the latter at the micro-structural (fiber-matrix) scale. Waas et al. (1990) have carefully monitored in real time the compressive damage initiation and propagation in a laminated plate through holographic interferometry and photomicrography of the hole surface, and have concluded that failure is initiated as a localized micro-buckling/kinking instability in the 0°-plies at the hole surface followed by delamination.

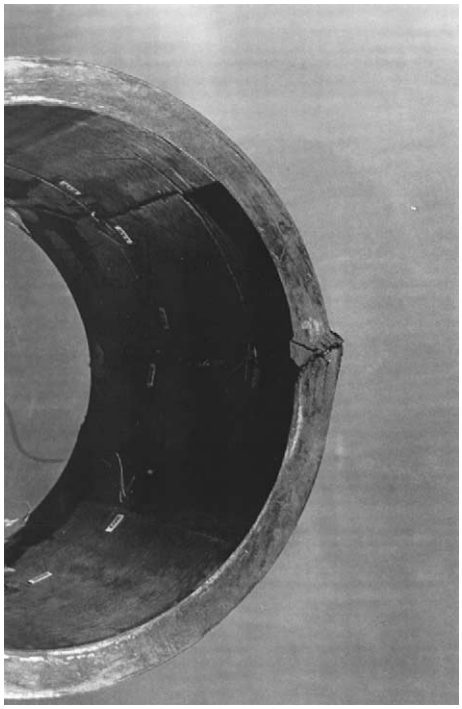

Fig. 1. Localized shear-crippling failure in a thick $[90_2/0]_k$ cylindrical shell tested under hydrostatic compression at NSWC, Carderock, MD.

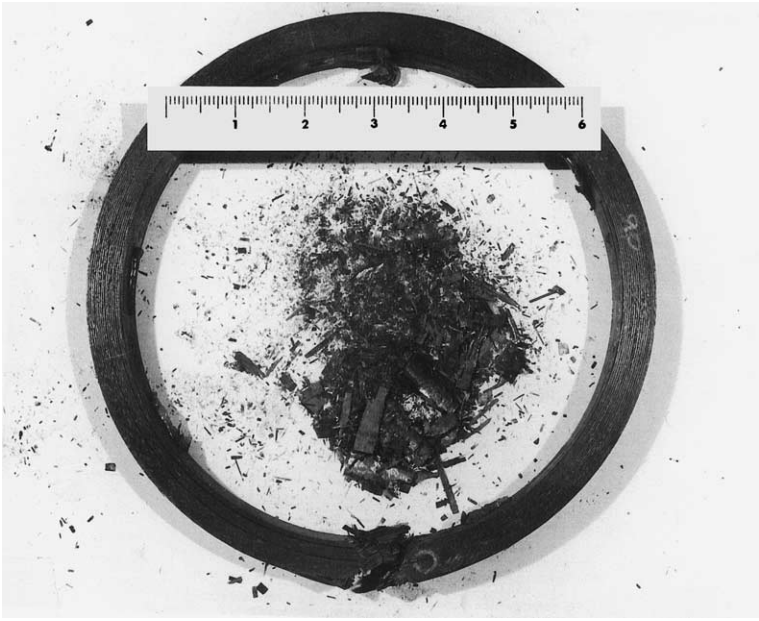

Fig. 2. Localized shear-crippling failure in a thick $[90_2/0]_k$ ring tested under hydrostatic compression at Alliants (formerly, Hercules), Inc., Magna, UT.

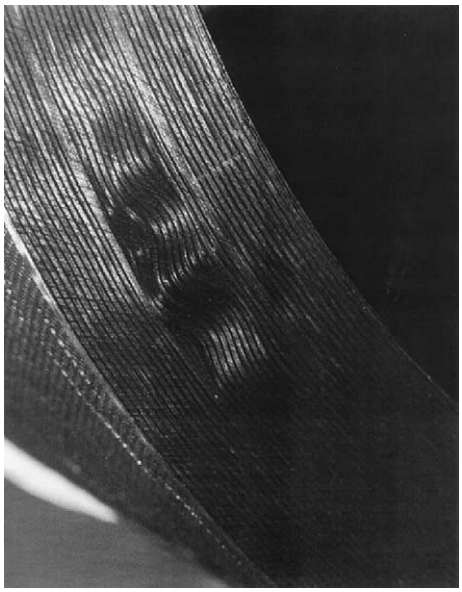

Fig. 3. Localized fiber waviness in a thick composite cylinder shell.

Chaudhuri (1991) has identified the formation and propagation of fiber kink bands at the microscopic level triggered by localized defects, such as fiber misalignment (see Fig. 3 for an extreme example), formed during the manufacturing process, leading to localized shear-crippling failures observed by Garala (1989) and Abdallah et al. (1990) and shown in Figs. 1 and 2, to be the dominant (lowest energy) compressive failure mode for the thick-section $[90_2/0]_m$ type composite cylinders. Initial fiber misalignment, ultimate fiber strain and the two transverse shear moduli, G_{LT} and G_{TT}, of the laminate, have been found to be the key parameters, limiting the compressive strength of the afore-mentioned thick-section composite laminates. Regardless of the event or sequence of events that may act as precursor(s), kink band formation, once triggered, will, in general, be the dominant (lowest energy) failure mode, especially in the presence of such defects as fiber waviness or misalignment, resin rich areas, etc. Numerical results for carbon/epoxy laminates demonstrate their extreme sensitivity to initial fiber misalignment defects, which are, at least partially, responsible for the lowering of the compressive strength of the thick cylinders tested by Garala (1989) and the observed scatter in his test data. These theoretical results have also been experimentally verified by Garala (1989). Various candidate sites for initiation of localized shear-crippling failures in laminated composite structural components, experimentally observed by Garala (1989), Abdallah et al. (1990), Starnes and Williams (1982) and others are shown in Fig. 4.

The afore-mentioned understanding of the microscopic behavior of carbon/epoxy composites notwithstanding, some serious questions remain to be addressed. Of utmost importance is the transition or missing link between micro-structural instability, such as kink band type failure at the fiber-matrix level (at the geometric scale of about 10 μm) investigated by Chaudhuri et al. (1996) and others on one hand, and macro-structural instability, such as buckling/post-buckling failure of a structural component, e.g., a ring or cylindrical shell (at the geometric scale of at least several cm's and larger). This transition, termed here meso-structural instability, is identified to occur at the ply level at the geometric scale of about at a minimum of some multiples of 130 μm (a ply thickness), and is the primary focus of the present investigation. In the interest of computational efficiency, about 38 such plies are lumped together to form a model layer in the present study, without any loss of generality of the issue at hand or of accuracy of the con-

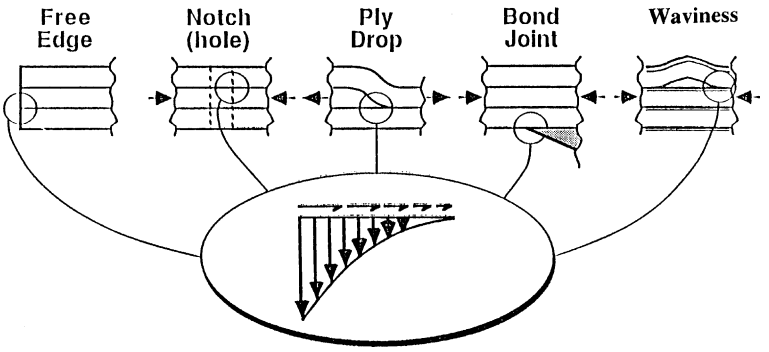

Fig. 4. Various initiation sites for localized shear-crippling failure in laminated composite structural components.

clusions to be drawn based on these numerical results. Of additional interest is the sensitivity of the response of a thick composite ring (infinitely long cylindrical shell) to nonlinear material property, as well as to geometrical defects such as dimple shaped local imperfections in addition to modal imperfections, e.g., out-of-roundness, which are apt to be generated during a large scale fabrication process of thick-section laminated shells.

In this connection, it is worthwhile to mention that the compressive response of a thin ring or shell structure is known to be primarily characterized by the stability of equilibrium at the macro-structural level. The loss of stability of an isotropic thin shell-type structure under external pressure has been studied extensively since the pioneering work of Koiter (1945), and is relatively well understood. An important ingredient of Koiter's theory is the investigation of the effect of a small imperfection whose shape is the same as that of a classical buckling mode. More recently, Abdelmoula et al. (1992) have investigated the effect of modal as well as local (dimple shaped) imperfections on the load carrying capacity of thin elastic isotropic cylindrical shells subjected to external pressure. Jamal et al. (1999) have investigated the influence of localized imperfections on the elastic buckling of a long cylindrical shell (with large Batdorf parameter) under axial compression by using a double scale analysis including interaction modes. Kim and Chaudhuri (in review) have investigated the influence of a localized imperfection on the elastic buckling of a thin cylindrical shell (with large Batdorf parameter) under hydrostatic pressure using a finite element analysis with fully nonlinear kinematic relations. Tvergaard and Needleman (1980) in relation to the compression failure of thin metallic structures, such as an elastic column on a softening (inelastic) foundation and an elastic–plastic plate have observed that "the final buckled configuration involves a localized buckling pattern, in contrast with the periodic deformation pattern associated with the critical buckling mode", and additionally, that the applied load–deflection curve attains a maximum or limit load point. Their finite element analysis of the elastic–plastic imperfect thin strip under axial compression shows the development of localization for the case of a low hardening material, whereas localization does not occur in the otherwise same plate of a high hardening material for which no limit load is reached. More recently, Tvergaard and Needleman (2000) have reexamined the post-bifurcation behavior of an axially compressed elastic–plastic cylindrical panel, and confirmed their previous conclusion with regards to the localization of buckling patterns reached for the afore-mentioned problems analyzed in their earlier work (Tvergaard and Needleman, 1980). A detailed review of the literature on localization of buckling pattern in elastic–plastic thin structural elements, localization of plastic flow, including shear band formation in solids and localized necking in biaxially stretched metal sheets, and cavitational (void growth) instabilities in elastic–plastic solids is available in Tvergaard (1999), and will not be repeated here in the interest of brevity. For other recent localization studies in buckling, the special issue of the journal "Chaos, Solitons and Fractals" (Xie, 2000) and references quoted therein may be consulted by interested readers.

A review of the literature suggests that the emergence of meso-structure (i.e., lamina level) related instability modes, such as interlaminar shear-crippling failures, experimentally observed by Starnes and Williams (1982) and Garala (1989) has not been investigated to the extent it deserves. Therefore, the primary objective of the present investigation is to fill this analytical gap, and to identify basic meso-structure-related mechanisms causing the afore-mentioned "premature" failure of the advanced composite rings under investigation.

Chaudhuri and Kim (1997) have investigated the roles of thickness (i.e., interlaminar shear/normal deformation) and modal imperfection in lowering the load carrying capability of an infinitely long (plane strain) thick symmetrically laminated cross-ply [90/0/90] cylindrical shell (ring) with linear material property. Numerical results on symmetrically laminated [90/0/90] moderately thick and thick (plane strain) rings with modal imperfections and made of linear elastic materials show that a limit point appears on the post-buckling equilibrium path, due to the effect of interlaminar shear deformation, significantly reducing the load carrying capacity (e.g., 72.6% in the case of $R_i/h = 6.0$) compared to their classical lamination theory (CLT) based linearized buckling loads. The appearance of a limit point on the elastic post-buckling equilibrium path is delayed as the inner radius to thickness ratio increases (i.e., as the effect of interlaminar shear/normal deformation decreases) from 6 to 60, and finally disappears in the very thin ring case ($R_i/h = 60$ and beyond), which is to be expected in accordance with the CLT. As has been discussed there, the appearance of a limit point on the elastic post-buckling equilibrium path is a measure of the effect of interlaminar shear/normal deformation on localization. This notwithstanding, the effect of material nonlinearity combined with that of localized imperfection on the details of the localization behavior in the context of interlaminar shear deformation at the lamina level has not been investigated, however.

In what follows, a nonlinear thick cylindrical shell finite element analysis is developed in order to obtain the discretized system equations. The present investigation includes all the nonlinear terms in the kinematic equations and utilizes the total Lagrangian formulation in the constitutive equations and incremental equilibrium equations. A cylindrically curved 16-node layer-element is used, which is based on an assumed quadratic displacement field (in surface-parallel coordinates) and the assumption of layerwise linear displacements distribution through thickness (LLDT). The Newton–Raphson iteration scheme in conjunction with Aitken acceleration is used to obtain the limit load. Beyond this load, the post-buckling behavior is obtained by an incremental displacement control scheme rather than the usual incremental force control scheme, when a limit point appears on the equilibrium path. In order to investigate localization of the buckling pattern, a modal in combination with a local or dimple shaped imperfection is selected. The combined effects of local/modal imperfections, interlaminar shear/normal deformation and nonlinear (hypoelastic) material property for the transverse shear modulus, G_{TT}, on the emergence of interlaminar shear-crippling type meso-structural instability modes, related to the localization phenomenon, are investigated. The classical approach which is concerned with the periodic buckling/post-buckling pattern, although deemed sufficient for the design of most thin elastic structures, is inadequate when it comes to localized failures (instabilities), such as those experimentally observed by Garala (1989) and Abdallah et al. (1990).

2. Three-dimensional kinematic relations for a thick imperfect cylindrical shell

Fig. 5 shows the schematic of a laminated cylindrical shell. Invoking the theory of parallel surfaces, the coefficients of the first fundamental differential quadratic form of a surface inside the ith layer of a laminated imperfect cylindrical shell can be written in terms of their bottom surface counterparts as follows:

$$g_x^{(i)}(z) = 1, \quad g_\beta^{(i)}(z) = \bar{g}_\beta^{(i)}\left(1 + \frac{z}{\rho^{(i)}}\right), \quad g_z^{(i)}(z) = 1. \tag{1}$$

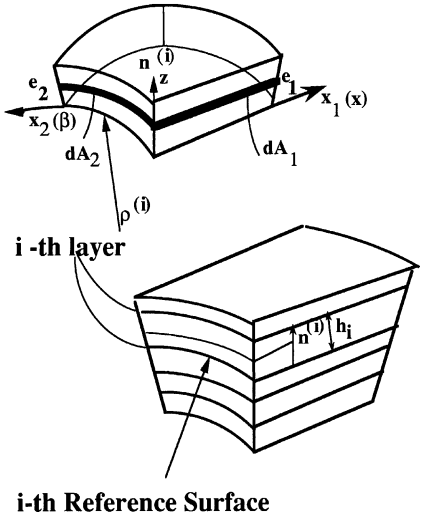

Fig. 5. Geometry of a laminated cylindrical shell (infinitesimal) element.

The components of the engineering nonlinear strain in terms of the physical components of the displacement vector at an arbitrary point inside the ith layer are obtained as follows:

$$\varepsilon_{11}^{(i)}(x,\beta,z)=\frac{\partial u^{(i)}}{\partial x}+\frac{1}{2}\left[\left(\frac{\partial u^{(i)}}{\partial x}\right)^2+\left(\frac{\partial v^{(i)}}{\partial x}\right)^2+\left(\frac{\partial w^{(i)}}{\partial x}\right)^2\right], \tag{2a}$$

$$\varepsilon_{22}^{(i)}(x,\beta,z)=\frac{1}{g_\beta^{(i)}}\left(\frac{\partial v^{(i)}}{\partial \beta}+w^{(i)}\right)+\frac{1}{2(g_\beta^{(i)})^2}\left[\left(\frac{\partial u^{(i)}}{\partial \beta}\right)^2+\left(\frac{\partial v^{(i)}}{\partial \beta}+w^{(i)}\right)^2+\left(\frac{\partial w^{(i)}}{\partial \beta}-v^{(i)}\right)^2\right], \tag{2b}$$

$$\varepsilon_{12}^{(i)}(x,\beta,z)=\frac{\partial v^{(i)}}{\partial x}+\frac{1}{g_\beta^{(i)}}\frac{\partial u^{(i)}}{\partial \beta}+\frac{1}{(g_\beta^{(i)})}\left[\frac{\partial u^{(i)}}{\partial x}\frac{\partial u^{(i)}}{\partial \beta}+\frac{\partial v^{(i)}}{\partial x}\left(\frac{\partial v^{(i)}}{\partial \beta}+w^{(i)}\right)+\frac{\partial w^{(i)}}{\partial x}\left(\frac{\partial w^{(i)}}{\partial \beta}-v^{(i)}\right)\right], \tag{2c}$$

$$\varepsilon_{33}^{(i)}(x,\beta,z)=\frac{\partial w^{(i)}}{\partial z}+\frac{1}{2}\left[\left(\frac{\partial u^{(i)}}{\partial z}\right)^2+\left(\frac{\partial v^{(i)}}{\partial z}\right)^2+\left(\frac{\partial w^{(i)}}{\partial z}\right)^2\right], \tag{2d}$$

$$\varepsilon_{13}^{(i)}(x,\beta,z)=\frac{\partial w^{(i)}}{\partial x}+\frac{\partial u^{(i)}}{\partial z}+\frac{\partial u^{(i)}}{\partial x}\frac{\partial u^{(i)}}{\partial z}+\frac{\partial v^{(i)}}{\partial x}\frac{\partial v^{(i)}}{\partial z}+\frac{\partial w^{(i)}}{\partial x}\frac{\partial w^{(i)}}{\partial z}, \tag{2e}$$

$$\varepsilon_{23}^{(i)}(x,\beta,z)=\frac{1}{g_\beta^{(i)}}\left(\frac{\partial w^{(i)}}{\partial \beta}-v^{(i)}\right)+\frac{\partial v^{(i)}}{\partial z}+\frac{1}{(g_\beta^{(i)})}\left[\frac{\partial u^{(i)}}{\partial \beta}\frac{\partial u^{(i)}}{\partial z}+\left(\frac{\partial v^{(i)}}{\partial \beta}+w^{(i)}\right)\frac{\partial v^{(i)}}{\partial z}+\left(\frac{\partial w^{(i)}}{\partial \beta}-v^{(i)}\right)\frac{\partial w^{(i)}}{\partial z}\right], \tag{2f}$$

where

$$g_\beta^{(i)}(z)=\bar{g}_\beta^{(i)}\left(1+\frac{z}{\rho^{(i)}}\right). \tag{3}$$

3. Linearized equations of motion and the method of virtual work

The second Piola–Kirchhoff stress tensor is conjugate to the Green–Lagrange strain tensor in that their properties are also invariant under rigid body motions. When the equilibrium of the body at time $t + \Delta t$ is first expressed using the principle of virtual displacements with tensor notation, the total Lagrangian formulation requires that

$$\int_{{}_0V} {}^{t+\Delta t}_{0}S_{ij}\,\delta\,{}^{t+\Delta t}_{0}\bar{\varepsilon}_{ij}\,{}^{0}\,\mathrm{d}V = {}^{t+\Delta t}\Re, \tag{4}$$

where the ${}^{t+\Delta t}_{0}S_{ij}$ and ${}^{t+\Delta t}_{0}\varepsilon_{ij}$ are the Cartesian components of the second Piola–Kirchhoff stress tensor and the total Green–Lagrange strain tensor defined at time $t + \Delta t$, respectively, referred to the initial configuration, while ${}^{t+\Delta t}\Re$ represents the external virtual work. Furthermore,

$${}^{t+\Delta t}_{0}S_{ij} = {}^{t}_{0}S_{ij} + {}_0S_{ij} \tag{5}$$

and

$${}^{t+\Delta t}_{0}\bar{\varepsilon}_{ij} = {}^{t}_{0}\bar{\varepsilon}_{ij} + {}_0\bar{\varepsilon}_{ij}, \qquad {}_0\bar{\varepsilon}_{ij} = {}_0\bar{e}_{ij} + {}_0\bar{\eta}_{ij}, \tag{6a, b}$$

where ${}^{t}_{0}S_{ij}$ and ${}_0S_{ij}$ represent components of the second Piola–Kirchhoff stress tensor defined at time t, and the incremental components of the same during the subsequent time step Δt, respectively, both referred to the initial configuration. The quantities ${}_0\bar{e}_{ij}$ and ${}_0\bar{\eta}_{ij}$ in Eq. (6b) denote the linear and the nonlinear incremental strains, respectively, that are referred to the initial configuration. The linear strain vector $\{{}_0\bar{e}_{ij}\}$ is here resolved into two parts that are the pure linear part $\{{}_0\bar{e}^{\mathrm{L}}_{ij}\}$, and the linearized part $\{{}_0\bar{e}^{\mathrm{N}}_{ij}\}$. The incremental constitutive relation, which relates the components of incremental stress and incremental strain both referred to the initial configuration, is given by

$${}_0S_{ij} = {}_0C_{\mathrm{ijrs}}\,{}_0\bar{\varepsilon}_{\mathrm{rs}} \tag{7}$$

in which ${}_0C_{\mathrm{ijrs}}$ is the incremental elastic stiffness (material property) tensor, referred to the initial configuration and represented as $[\overline{Q}]$ in matrix notation (see Appendix A and also refer to Fig. 6). Substitution of

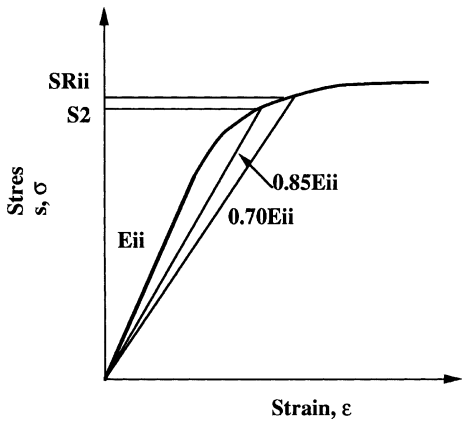

Fig. 6. Definition of parameters in Ramberg–Osgood representation of stress–strain curves.

Eqs. (5)–(7) into the left hand side of Eq. (4) finally yields the equations needed for the finite element formulation. The details are available in Chaudhuri and Kim (1997).

Because the variation in the strain components is equivalent to the virtual strains, the right hand side of Eq. (4) is the virtual work done when the body is subjected to a virtual displacement at time $t + \Delta t$. The corresponding virtual work is given by

$$^{t+\Delta t}\Re = \int_{^{t+\Delta t}S} {}^{t+\Delta t}f_i^S \, \delta \mathbf{v}_i^{S\,t+\Delta t} \mathrm{d}S, \tag{8a}$$

where the $^{t+\Delta t}f_i^S$ is the surface force vectors applied on the surface S at time $t + \Delta t$, and $\delta_0 v_i^S$ is the ith component of the incremental virtual displacement vector evaluated on the loaded surface. When the hydrostatic pressure is applied, the loading-path is always deformation-dependent, which requires that the load vector should be evaluated at the current configuration. The external virtual work can, however, be approximated to sufficient accuracy using the intensity of loading corresponding to time $t + \Delta t$, integrated over the surface area, $^{t+\Delta t}S^{(k-1)}$ calculated at the $(k-1)$th iteration (see Section 5) as follows:

$$^{t+\Delta t}\Re = \int_{^{t+\Delta t}S^{(k-1)}} {}^{t+\Delta t}f_i^S \, \delta_0 v_i^{S\,t+\Delta t} \mathrm{d}S. \tag{8b}$$

4. Isoparametric finite element discretization

In this section, a general nonlinear displacement-based finite element formulation is presented. The basic steps in the derivation of finite element equations are to select the interpolation functions of the displacements and the element coordinates. Because the new element coordinates are obtained by adding the element displacements to the original coordinates in the incremental analysis, the same interpolations can be employed for the displacements and coordinates. In the present study, 16-node quadrilateral elements (Fig. 7) are employed because of their computational efficiency, as compared to their lower-order linear counterparts, which are too stiff to model the shear deformation of each lamina in the laminate. The details are available in Chaudhuri and Kim (1997), and are, therefore, omitted here in the interest of brevity of presentation.

On computing the left and right sides of Eqs. (4) and (8) as sums of integrals over the volume and areas of all finite elements, followed by equating them, and incorporating the boundary conditions, the principle of virtual displacement, in conjunction with the total Lagrangian formulation, is invoked to obtain the incremental equations of motion as follows:

$$[\mathbf{K}_\mathrm{L}]\{{}_0\mathbf{V}\} + [\mathbf{K}_\mathrm{N}]\{{}_0\mathbf{V}\} = \{\mathbf{f}_\mathrm{L}\} - \{\mathbf{f}_\mathrm{N}\}, \tag{9}$$

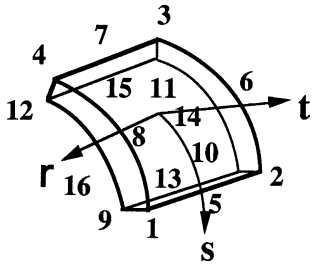

Fig. 7. A 16-node curvilinear side surface-parallel quadratic isoparametric cylindrical shell element.

where

$$[\mathbf{K}_{\mathrm{L}}] = \sum_{m=1}^{N_{\mathrm{L}}} \sum_{k=1}^{N_{\mathrm{S}}} \int_{S^{(m)}} \int_{h_{k-1}}^{h_k} ([B_{\mathrm{LL}}^{(k)}][T_{\mathrm{BT}}^{(k)}][\Phi])^{\mathrm{T}} [\overline{Q}^{(k)}][B_{\mathrm{LL}}^{(k)}][T_{\mathrm{BT}}^{(k)}][\Phi] \rho^{(k)} \, \mathrm{d}z \, \mathrm{d}S, \tag{10a}$$

$$\begin{aligned}[\mathbf{K}_{\mathrm{N}}] = {} & 2 \sum_{m=1}^{N_{\mathrm{L}}} \sum_{k=1}^{N_{\mathrm{S}}} \int_{S^{(m)}} \int_{h_{k-1}}^{h_k} ([B_{\mathrm{LL}}^{(k)}][T_{\mathrm{BT}}^{(k)}][\Phi])^{\mathrm{T}} [\overline{Q}^{(k)}][B_{\mathrm{LN}}^{(k)}][T_{\mathrm{BT}}^{(k)}][\Phi] \rho^{(k)} \, \mathrm{d}z \, \mathrm{d}S \\ & + \sum_{m=1}^{N_{\mathrm{L}}} \sum_{k=1}^{N_{\mathrm{S}}} \int_{S^{(m)}} \int_{h_{k-1}}^{h_k} ([B_{\mathrm{LN}}^{(k)}][T_{\mathrm{BT}}^{(k)}][\Phi])^{\mathrm{T}} [\overline{Q}^{(k)}][B_{\mathrm{LN}}^{(k)}][T_{\mathrm{BT}}^{(k)}][\Phi] \rho^{(k)} \, \mathrm{d}z \, \mathrm{d}S \\ & + \sum_{m=1}^{N_{\mathrm{L}}} \sum_{k=1}^{N_{\mathrm{S}}} \int_{S^{(m)}} \int_{h_{k-1}}^{h_k} ([B_{\mathrm{NN}}^{(k)}][T_{\mathrm{BT}}^{(k)}][\Phi])^{\mathrm{T}} [{}_0^t \widehat{S}^{(k)}][B_{\mathrm{NN}}^{(k)}][T_{\mathrm{BT}}^{(k)}][\Phi] \rho^{(k)} \, \mathrm{d}z \, \mathrm{d}S, \end{aligned} \tag{10b}$$

$$\{\mathbf{f}_{\mathrm{L}}\} = \sum_{m=1}^{N_{\mathrm{L}}} \int_{S^{(m)}} ([B_{\mathrm{LL}}^{(N_{\mathrm{S}})}][T_{\mathrm{BT}}^{(N_{\mathrm{S}})}][\Phi])^{\mathrm{T}} \begin{Bmatrix} \mathbf{n}^{N_{\mathrm{S}}+1} \\ \mathbf{0} \end{Bmatrix} P_{\mathrm{r}} \rho^{(N_{\mathrm{S}}+1)} \, \mathrm{d}S, \tag{11a}$$

$$\{\mathbf{f}_{\mathrm{N}}\} = \sum_{m=1}^{N_{\mathrm{L}}} \sum_{k=1}^{N_{\mathrm{S}}} \int_{S^{(m)}} \int_{h_{k-1}}^{h_k} ([B_{\mathrm{LL}}^{(k)}][T_{\mathrm{BT}}^{(k)}][\Phi])^{\mathrm{T}} \{{}_0^t \overline{S}^{(k)}\} \rho^{(k)} \, \mathrm{d}z \, \mathrm{d}S \tag{11b}$$

and

$$\begin{aligned}\{{}_0\mathbf{V}\}^{\mathrm{T}} = \{ & {}_0U_{b1}^{(1)} \bullet \bullet_0 U_{b8}^{(1)} {}_0V_{b1}^{(1)} \bullet \bullet_0 V_{b8}^{(1)} {}_0W_{b1}^{(1)} \bullet \bullet_0 W_{b8}^{(1)} {}_0U_{t1}^{(1)} \bullet \bullet_0 U_{t8}^{(1)} {}_0V_{t1}^{(1)} \bullet \bullet_0 V_{t8}^{(1)} {}_0W_{t1}^{(1)} \bullet \bullet_0 W_{t8}^{(1)} {}_0U_{b1}^{(i)} \\ & \bullet \bullet_0 U_{b8}^{(i)} {}_0V_{b1}^{(i)} \bullet \bullet_0 V_{b8}^{(i)} {}_0W_{b1}^{(i)} \bullet \bullet_0 W_{b8}^{(i)} {}_0U_{t1}^{(i)} \bullet \bullet_0 U_{t8}^{(i)} {}_0V_{t1}^{(i)} \bullet \bullet_0 V_{t8}^{(i)} {}_0W_{t1}^{(i)} \bullet \bullet_0 W_{t8}^{(i)} {}_0U_{b1}^{(N)} \\ & \bullet \bullet_0 U_{b8}^{(N)} {}_0V_{b1}^{(N)} \bullet \bullet_0 V_{b8}^{(N)} {}_0W_{b1}^{(N)} \bullet \bullet_0 W_{b8}^{(N)} {}_0U_{t1}^{(N)} \bullet \bullet_0 U_{t8}^{(N)} {}_0V_{t1}^{(N)} \bullet \bullet_0 V_{t8}^{(N)} {}_0W_{t1}^{(N)} \bullet \bullet_0 W_{t8}^{(N)} \}. \end{aligned} \tag{12}$$

It may be noted that the total number of elements, N equals $N_{\mathrm{L}} * N_{\mathrm{S}}$.

5. Iterative solution strategy

Because the nodal point forces at time $t + \Delta t$ depend nonlinearly on the nodal point displacements, it is necessary to iterate for obtaining a reasonably accurate solution of Eq. (9). The most frequently used iteration scheme for solutions of nonlinear finite element equations is the Newton–Raphson iteration because reformations and triangularizations of stiffness matrices at selective load and iteration steps are more computationally efficient without a significant loss of accuracy. In the Newton–Raphson method, only the stress force vector (i.e., the right hand side of Eq. (9)) is modified without changing the stiffness matrix after each iteration of a certain load step, and the following algorithm for solving Eq. (9) is developed:

$$([\mathbf{K}_{\mathrm{L}}] + {}^t[\mathbf{K}_{\mathrm{N}}])\{{}_0\mathbf{V}\}^{(i)} = {}^{t+\Delta t}\{f_{\mathrm{L}}\} - {}^{t+\Delta t}\{f_{\mathrm{N}}\}^{(i-1)}, \tag{13}$$

$${}^{t+\Delta t}\{\mathbf{V}\}^{(i)} = {}^{t+\Delta t}\{\mathbf{V}\}^{(i-1)} + [A]^{(i)}\{{}_0\mathbf{V}\}^{(i)}, \tag{14}$$

with the initial conditions ${}^{t+\Delta t}\{f_{\mathrm{N}}\}^{(0)} = {}^t\{f_{\mathrm{N}}\}$, and ${}^{t+\Delta t}\{\mathbf{V}\}^{(0)} = {}^t\{\mathbf{V}\}$, where the index i denotes the number of iterations performed in a certain time step Δt. The subscripts 'L' and 'N' denote the linear and the nonlinear components evaluated at the time t, while the diagonal matrix $[A]$ is Aitken acceleration factor to increase the convergence rate. Eq. (13) is the computational equivalent of Eq. (9). Furthermore, in the computer program, the process of the assemblage for the total stiffness matrix can be divided into two groups: the first group contains linear elements, where the stiffness matrices of each individual element are only calculated at the first load step and remain unchanged during whole loading process. The second one

refers to the nonlinear elements where nonlinear stiffness matrices of the element can be evaluated at the first iteration of each load step with nonlinear force vectors being evaluated at each iteration of every load step using the contributions of current displacements or stresses. The applied force and the stress force vectors (i.e., ${}^{t+\Delta t}\{f_L\}$ and ${}^{t+\Delta t}\{f_N\}^{(i-1)}$ in Eq. (13)) are calculated according to Eq. (11) as follows:

$$ {}^{t+\Delta t}\{\mathbf{f}_L\} = \sum_{m=1}^{N_L} \int_{S^{(m)}} ([{}^{t+\Delta t}B_{LL}^{(N_S)}][{}^{t+\Delta t}T_{BT}^{(N_S)}][\Phi])^T \begin{Bmatrix} {}^{t+\Delta t}\mathbf{n}^{(N_S+1)} \\ \mathbf{0} \end{Bmatrix} P_r \rho^{(N_S+1)}\, {}^{t+\Delta t}\mathrm{d}S \tag{15} $$

and

$$ {}^{t+\Delta t}\{\mathbf{f}_N\}^{(i-1)} = \sum_{m=1}^{N_L} \sum_{k=1}^{N_S} \int_{S^{(m)}} \int_{h_{k-1}}^{h_k} ([{}^{t+\Delta t}B_{LL}^{(k)}]^{(i-1)}[{}^{t+\Delta t}T_{BT}^{(k)}]^{(i-1)}[\Phi])^T \{{}^{t+\Delta t}_{0}\overline{S}^{(k)}\}^{(i-1)} \rho^{(k)}\, \mathrm{d}z\, \mathrm{d}S \tag{16} $$

in which $[{}^{t+\Delta t}B_{LL}^{(k)}]^{(i-1)}[{}^{t+\Delta t}T_{BT}^{(k)}]^{(i-1)}$ is a linear differential operator of the kth layer evaluated at $(i-1)$th iteration of each load step. The 6×1 element stress vector $\{{}^{t+\Delta t}_{0}\overline{S}^{(k)}\}^{(i-1)}$ can be calculated by generalizing the linear elastic relations, $\{{}^{t+\Delta t}_{0}\overline{S}^{(k)}\}^{(i-1)} = [{}^{t}_{0}\overline{Q}^{(k)}]^{(i-1)}\{{}^{t+\Delta t}_{0}\bar{\varepsilon}^{(k)}\}^{(i-1)}$ (Hooke's law in infinitesimal displacement conditions) for the linear material because the second Piola–Kirchhoff stress and Green–Lagrangian strain tensors are invariant under rigid body motions in large displacement and rotation. In the case of a nonlinear elastic material, the element stress vector $\{{}^{t+\Delta t}_{0}\overline{S}^{(k)}\}^{(i-1)}$ can be simply evaluated by subsequently adding incremental stresses at each iteration to stresses calculated at the first iteration of the current load step and denoted by

$$ \{{}^{t+\Delta t}_{0}\overline{S}^{(k)}\}^{(i-1)} = \{{}^{t}_{0}\overline{S}^{(k)}\}^{(0)} + \sum_{j=1}^{i-1} \{\Delta\overline{S}^{(k)}\}^{(j)}, \tag{17} $$

where $\{{}^{t}_{0}\overline{S}^{(k)}\}^{(0)}$ is the total second Piola–Kirchhoff stress vector in an element of the kth layer at time t, and $\{\Delta\overline{S}^{(k)}\}^{(j)}$ is the incremental stress vector created during the jth iteration. The first term on the right hand side of Eq. (17) is equivalent to its counterpart in Eq. (5). Furthermore, the incremental stress can be denoted by

$$ \{\Delta\overline{S}^{(k)}\}^{(j)} = [{}^{t}_{0}\overline{Q}^{(k)}]^{(j)}\{\Delta\bar{\varepsilon}^{(k)}\}^{(j)}, \tag{18} $$

where $[{}^{t}_{0}\overline{Q}^{(k)}]^{(j)}$ and $\{\Delta\bar{\varepsilon}^{(k)}\}^{(j)}$ are tangent modulus matrix at the current load step and incremental strain components generated during the jth iteration, respectively. It may be noted that the same procedure can be applied to evaluate the 9×9 element stress matrix $[{}^{t}_{0}\widehat{S}^{(k)}]$ that appears in the nonlinear stiffness matrix of Eq. (10b).

In actual computer programming, the active columns and the addresses of the diagonal elements of the total stiffness matrix are stored effectively in an one-dimensional array, and an effective subroutine COLSOL (active column solver) is used to finally obtain the incremental displacement for the unbalanced force, ${}^{t+\Delta t}\Delta R^{(i-1)} = {}^{t+\Delta t}\{f_L\} - {}^{t+\Delta t}\{f_N\}^{(i-1)}$ in the $(i-1)$th iteration. The iteration is continued until the out-of-balance load vector and the displacement increments are sufficiently small, i.e., the iteration scheme is terminated at the current load step and moves to the next load step, when the force convergence criterion,

$$ \frac{\|{}^{t+\Delta t}\{f_L\} - {}^{t+\Delta t}\{f_N\}^{(i)}\|}{\|{}^{t+\Delta t}\{f_L\} - {}^{t}\{f_L\}\|} < \varepsilon_f \tag{19a} $$

and the energy convergence criterion,

$$ \frac{\{{}_0\mathbf{V}\}^{(i)T}({}^{t+\Delta t}\{f_L\} - {}^{t+\Delta t}\{f_N\}^{(i-1)})}{\{{}_0\mathbf{V}\}^{(1)T}({}^{t+\Delta t}\{f_L\} - {}^{t}\{f_L\})} < \varepsilon_e \tag{19b} $$

are simultaneously satisfied, where ε_f and ε_e are preset force and energy tolerances, while $\|\cdot\|$ denotes the Euclidean norm of the column vector. The Newton–Raphson method with a relatively large value of the load increment requires a number of iterations in the nonlinear regime. Otherwise, it may introduce serious errors and, indeed, diverge from the exact solution. Therefore, a rather small load increment would be necessary in the nonlinear regime. It may, however, be noted that the larger value of load increment is recommended, with a specified accuracy, for the linear regime, in the interest of computational efficiency.

The prediction of nonlinear structural behavior by the Newton–Raphson method is successfully achieved before the critical (limit) point of the solution, because the residual force vector and the gradient of the total system matrix do not change in sign drastically; i.e., physically, the total stiffness matrix monotonically decreases in the present investigation as the applied load is increased up to the limit load. In practice, during the solution process of the system, the stiffness matrix may approach singularity at the critical point, in which case the Newton-type method generally fails to give satisfactory results because of the multiple admissible solutions for a single value of load. It is necessary to modify the standard form of the Newton-type method, if it is employed to trace the post-buckling solution. The technique necessary to modify this method, based on displacement increment, is therefore employed beyond the critical (limit) point, which is shown to be efficient and reliable. The details of this important procedure are presented in Appendix C.

6. Results and discussion

Before undertaking investigations on meso-structure-related instability problems, a class of simpler macrostructural deformation and instability problems (e.g., isotropic and two layer [0/90] cylindrical panels with linear material property) had earlier been investigated to check the accuracy of the present theoretical development and the resulting finite element code, Nonlinear Laminated Shell Analysis with Meso-structure Program (NLSAMP). The issues of validity of the present LLDT based nonlinear incremental formulation (developed earlier), and assessment of the convergence characteristics of the present 16 node layer element were addressed for shallow homogeneous isotropic and cross-ply [0/90] panels in the absence of imperfections. Also addressed was the issue of accuracy of the von Karman nonlinear strain assumption which was found to overestimate transverse displacements in the advanced nonlinear regime. The results of these studies are available in Hsia and Chaudhuri (1996), Kim and Chaudhuri (1995), and Chaudhuri and Hsia (1998, 1999), and hence will not be repeated here in the interest of brevity.

Example: A thick symmetrically laminated cross-ply [90/0/90] (plane strain) ring (infinitely long cylindrical shell)

This study primarily addresses the problem of nonlinear (both geometric and material) post-buckling behavior of a thick symmetrically laminated cross-ply [90/0/90] (plane strain) ring (infinitely long cylindrical shell). First, the effect of a modal imperfection on the response of the laminated ring is presented (Chaudhuri and Kim, 1997), which serves as a baseline solution for comparison with that of a combined local and modal imperfection. A modal or harmonic imperfection is generally given by

$$r_0(\theta) = R_i - W_0 \cos\left(\frac{R_i\theta}{q_c}\right), \tag{20}$$

where $r_0(\theta)$ is the distance from the central axis of the perfect cylinder/ring to the inner surface of the imperfect cylinder/ring, and q_c is the wavelength of a classical buckling mode in the circumferential direction. For mode 2 of classical buckling of a ring (see Fig. 8(b)), Eq. (20) reduces to

$$r_0(\theta) = R_i - W_0 \cos(2\theta). \tag{21}$$

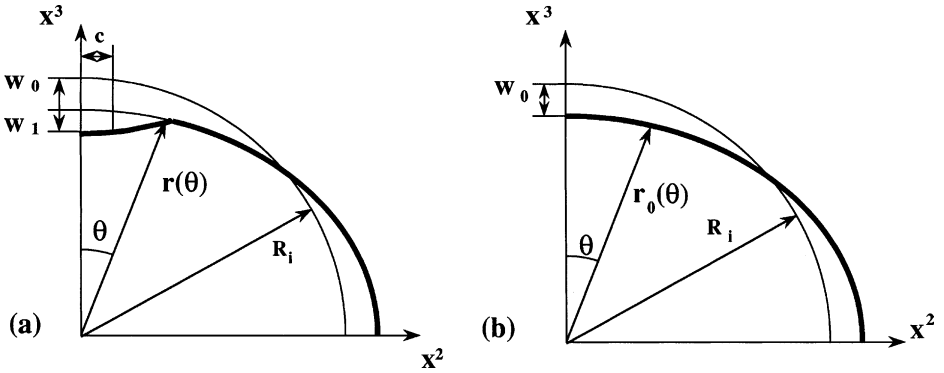

Fig. 8. Shape of a ring with (a) combined local/modal and (b) only modal imperfection.

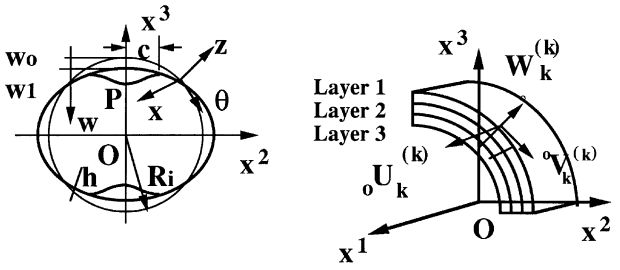

NS= 3

Geometric Properties :

Ri = 8.89 cm (3.5 in) ;

L = 1.356 cm (0.534 in);

Ri / h = 6.0;

wo/Ri = 0.005 and c = 2.54 cm (1.0 in)

w1 / Ri = 0.000, 0.05, 0.1, 0.2, 0.5

Fig. 9. Nomenclature and geometry of a (plane strain) [90/0/90] ring with a combined modal/local imperfection.

The geometry of the inner surface of a laminated ring with a modal imperfection, is described in detail in Fig. 8(b), while Fig. 8(a) depicts the same with combined local/modal imperfections. The inner radius (R_i) and thickness (h) of the [90/0/90] cross-ply (plane strain) ring are 8.89 cm (3.5 in.) and 1.48 cm (0.583 in.), respectively. The three-layer ring geometry with combined local/modal imperfections, of which the modal imperfection is a special case, is described in detail in Fig. 9.

Fiber orientation angles 90° and 0° represent the hoop and axial directions, respectively, of the cylinder/ring. The orthotropic lamina material properties for a Narmco 5605 graphite-epoxy composite under compression are as follows (see Appendix C, Jones, 1998):

$$E_{LL} = 124.11 \text{ GPa } (18.0 \text{ Msi}), \quad E_{TT} = 10.69 \text{ GPa } (1.55 \text{ Msi}), \quad \nu_{LT} = 0.575,$$
$$G_{LT} = 5.86 \text{ GPa } (0.85 \text{ Msi}), \quad G_{TT} = 3.10 \text{ GPa } (0.45 \text{ Msi}).$$

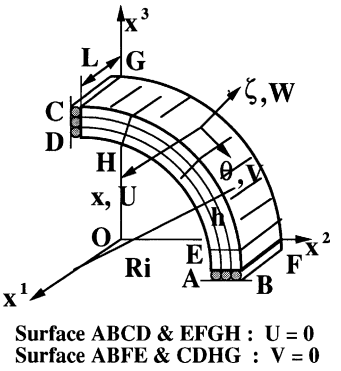

Fig. 10. Finite element model of a [90/0/90] cylindrical ring.

The finite element model of a quarter of the plane strain (perfect) ring along with the prescribed boundary conditions is presented in Fig. 10, the imperfect ones being similar with progressively more refined mesh toward and in the vicinity of the localized dimple (not shown here). Double symmetry conditions permit every model under consideration to be limited to only a quarter of the ring such that the corresponding surface-parallel displacements vanish along the center lines and the buckled shapes are assumed to be symmetric. As a result, a cylinder geometry with plane strain constraint has been chosen in the present investigation, which has, in the absence of any geometric imperfection, an inner surface radius $\rho^{(1)} = R_i$. Because the loading and geometric symmetries are assumed, boundary conditions on the surfaces in Fig. 10 can be prescribed as follows:

Geometric symmetry

$$\text{on the surfaces ABFE and CDHG}: \quad {}_0v(x,0,\zeta) = 0 \quad \text{and} \quad {}_0v(x,\pi/2,\zeta) = 0, \tag{22a}$$

$$\text{on the surface EHGF}: \quad {}_0u(0,\beta,\zeta) = 0. \tag{22b}$$

Loading symmetry

$$\text{Traction force on the surface BCGF}: \quad f_i^S = p(x,\beta,\rho^{(N_S+1)})n_i^{(N_S+1)}. \tag{23}$$

The plane strain condition in the three-dimensional model is obtained by applying the displacement constraints as shown below:

$$\begin{aligned} {}_0u_1^{(i)} &= {}_0u_2^{(i)} = {}_0u_3^{(i)} = {}_0u_4^{(i)} = {}_0u_5^{(i)} = {}_0u_6^{(i)} = {}_0u_7^{(i)} = {}_0u_8^{(i)} = {}_0u_9^{(i)} = {}_0u_{10}^{(i)} = {}_0u_{11}^{(i)} = {}_0u_{12}^{(i)} = {}_0u_{13}^{(i)} = {}_0u_{14}^{(i)} \\ &= {}_0u_{15}^{(i)} = {}_0u_{16}^{(i)} = 0, \end{aligned} \tag{24a}$$

$$\begin{aligned} &{}_0v_1^{(i)} = {}_0v_2^{(i)} = {}_0v_5^{(i)}, \quad {}_0v_9^{(i)} = {}_0v_{10}^{(i)} = {}_0v_{13}^{(i)}, \quad {}_0v_3^{(i)} = {}_0v_4^{(i)} = {}_0v_7^{(i)}, \quad {}_0v_{11}^{(i)} = {}_0v_{12}^{(i)} = {}_0v_{15}^{(i)}, \quad {}_0v_6^{(i)} = {}_0v_8^{(i)}, \\ &{}_0v_{14}^{(i)} = {}_0v_{16}^{(i)}, \end{aligned} \tag{24b}$$

$$\begin{aligned} &{}_0w_1^{(i)} = {}_0w_2^{(i)} = {}_0w_5^{(i)}, \quad {}_0w_9^{(i)} = {}_0w_{10}^{(i)} = {}_0w_{13}^{(i)}, \quad {}_0w_3^{(i)} = {}_0w_4^{(i)} = {}_0w_7^{(i)}, \quad {}_0w_{11}^{(i)} = {}_0w_{12}^{(i)} = {}_0w_{15}^{(i)}, \quad {}_0w_6^{(i)} = {}_0w_8^{(i)}; \\ &{}_0w_{14}^{(i)} = {}_0w_{16}^{(i)}, \end{aligned} \tag{24c}$$

where the superscript, i, denotes element number.

Fig. 11 shows a plot of p^*, the hydrostatic pressure, p, normalized by classical buckling pressure of its perfect counterpart, p_{cr}, versus the normalized displacement, $w^* = -w/(R_i - w_0)$ at $\theta = 0°$, of the thick

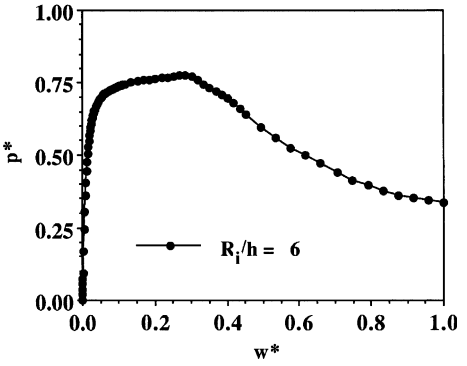

Fig. 11. Computed equilibrium paths of a thick ($R_i/h = 6$) composite [90/0/90] ring with only modal imperfection ($w_0 = 0.005R_i$).

[90/0/90] ring ($R_i/h = 6$, $w_0 = 0.005R_i$ and linear material property). This plot is the same as Fig. 13 from Chaudhuri and Kim (1997), the ordinate axis of which was labeled wrong, which is corrected here.

Fig. 12(a) exhibits the variation of the normalized radial distance of the deformed inner surface, $R_0^*(\theta) = R_0(\theta)(R_i - w_0)$, measured from the center of the ring during the initial pressurization process with $p^{**} = p/p_{max}$ in the range of 0–0.3157, which corresponds to the rising branch of the pressure–deflection curve of Fig. 11. Fig. 13(a) exhibits the same variation just before and at the time maximum pressure is reached, i.e., p^{**} being in the range of 0.9914–1.0, which corresponds to the peak of the pressure–deflection curve of Fig. 11, while Fig. 14(a) displays the same for the falling (unphysical) branch. Figs. 12(b), 13(b) and 14(b) show through the thickness distribution of the circumferential displacement at three locations, $\theta = 9°$, 45° and 81°, respectively, along the circumferential direction of the same ring. At the initial stage of loading, the maximum transverse deflection variation with the increase of load occurs around $\theta = 0°$, while the corresponding nodal line of the deformed shape is maintained at $\theta = 90°$ (Fig. 12(a)) in the case of the thick cross-ply ring under investigation, which is in marked contrast with what happens in the case of a thin cylindrical long shell (plane string ring), where the nodal line is located at $\theta = 45°$. This result implies that the thick [90/0/90] ring is susceptible to deform locally even in the presence of a modal imperfection, e.g., out-of-roundness. On the other hand, the undeformed normal of each section located at $\theta = 9°$, 45° and 81° along the circumferential direction of the thick [90/0/90] ring remains after deformation more or less

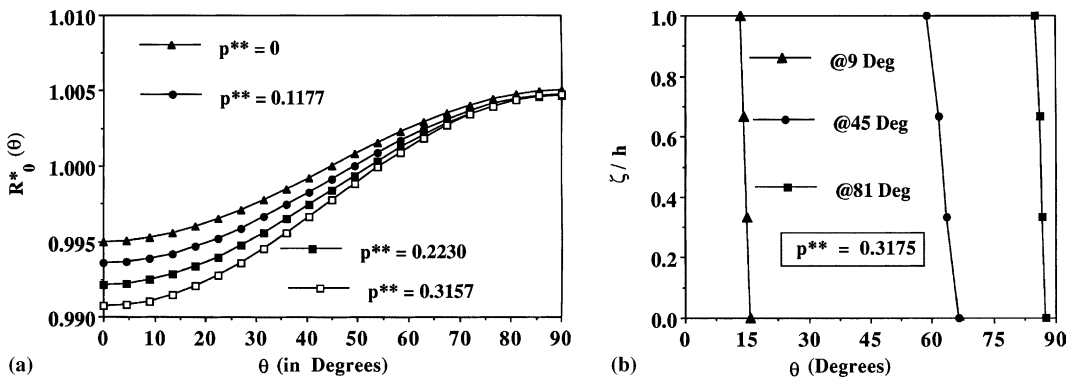

Fig. 12. Displacement patterns (rising pressure) of a thick composite [90/0/90] ring along the circumferential direction ($R_i/h = 6.0$, $w_0 = 0.005R_i$, linear elastic material): (a) normalized radial coordinate vs. angle and (b) normalized circumferential displacements vs. angle.

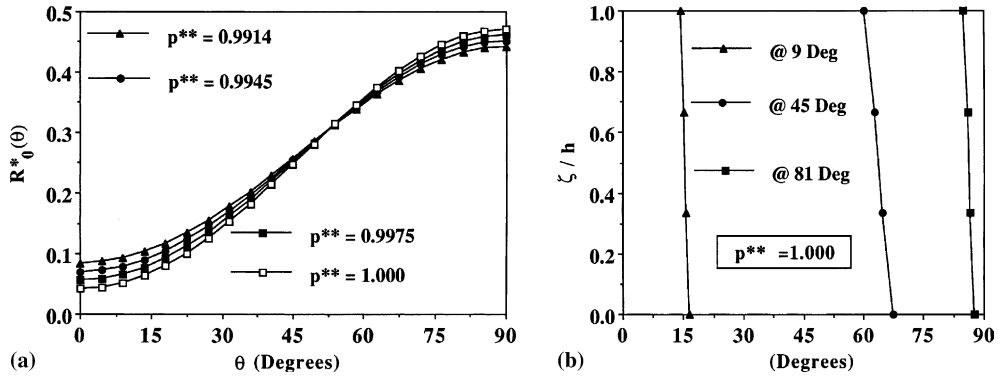

Fig. 13. Displacement patterns (near peak pressure) of a thick composite [90/0/90] ring along the circumferential direction ($R_i/h = 6.0$, $w_0 = 0.005R_i$, linear elastic material): (a) normalized radial coordinate vs. angle and (b) normalized circumferential displacements vs. angle.

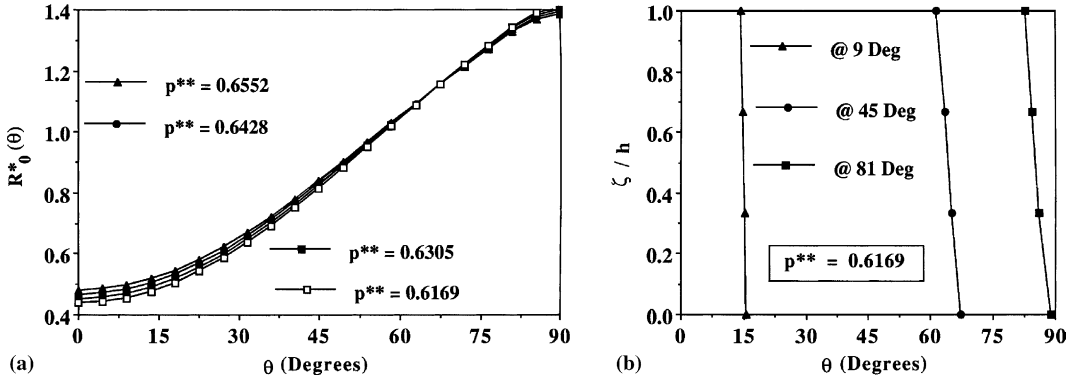

Fig. 14. Displacement patterns (falling pressure) of a thick composite [90/0/90] ring along the circumferential direction ($R_i/h = 6.0$, $w_0 = 0.005R_i$, linear elastic material): (a) normalized radial coordinate vs. angle and (b) normalized circumferential displacements vs. angle.

straight through the thickness as the applied hydrostatic pressure is increased (Fig. 12(b)). As the maximum pressure is reached, the nodal line travels from $\theta = 90°$ up to $\theta = 50°$, while the transverse deflection at $\theta = 90°$ starts to increase slightly with the increase of the load (Fig. 13(a)). It is also evident from Fig. 13(b) that the undeformed normal of each layer deforms linearly as before except around $\theta = 81°$. Finally, the nodal line does not move further and both the sections, $\theta = 0°$ and $\theta = 90°$ deflects in the opposite directions up to the ultimate point of the pressure–displacement plot (Fig. 14(a)). It is also seen that the first-order shear deformation theory (FSDT) appears to be adequate to predict an accurate load–displacement solution of the cross-ply composite (plane strain) ring with modal or harmonic imperfection and of linear material property, because the circumferential displacement variation through the thickness remains more or less linear during the whole loading process.

It may be noted that the computed deformed shapes of the composite [90/0/90] ring in the radial direction shown in Figs. 12–14 earlier for different hydrostatic pressures (where the normalization with respect to the maximum pressure, p_{max}, is used) reveal an absence of shear-crippling type post-bifurcation localization of the deformation pattern, which will require additional consideration. Tvergaard and Needleman (1980, 2000) have studied the post-bifurcation localization process by introducing a small localized

imperfection superimposed upon the modal type of imperfection. The initiation of the shear-crippling process in a thick cross-ply ring is then a consequence of the occurrence of the limit (maximum) point in the pressure (force)-deflection curve. Segments along the circumference of the ring, which are slightly weaker than the rest, attain the maximum first and shear-cripple or kink under falling pressure, while the remainder of the ring "unloads" without shear crippling.

For the purpose of illustration, the afore-mentioned weakening effect is represented by the presence of two symmetrically placed dimple type of imperfections superimposed upon the modal type imperfection shown in Fig. 8(a) in a manner similar to Tvergaard and Needleman (1980, 2000). The initial imperfections under consideration have (a) local shapes as well as (b) idealized modal shapes corresponding to classical buckling modes for a ring. The radial coordinate of a ring with local imperfections is described as follows:

$$r(\theta) = R_{\mathrm{i}} - \left[w_0 + w_1 \exp\left\{ -\left(\frac{R_{\mathrm{i}}\theta}{c} \right)^2 \right\} \right] \cos\left(\frac{R_{\mathrm{i}}\theta}{q_{\mathrm{c}}} \right), \tag{25}$$

where $r(\theta)$ is the distance from the central axis of the corresponding perfect cylinder/ring to the inner surface of the imperfect ring with combined modal and local imperfections, while w_1 represents the amplitude and c is the extent of the local imperfection. For mode 2 of classical buckling of a ring (see Figs. 8(a) and 9), Eq. (25) reduces to

$$r(\theta) = R_{\mathrm{i}} - \left[w_0 + w_1 \exp\left\{ -\left(\frac{R_{\mathrm{i}}\theta}{c} \right)^2 \right\} \right] \cos(2\theta). \tag{26}$$

It may be noted that the idealized modal imperfections, given above by Eqs. (20) and (21) can be obtained through substitution of $w_1 = 0$ and/or $c = 0$ in Eqs. (25) and (26), respectively. The arc length c and modal imperfection amplitude, w_0, are kept here constants at 2.54 cm (1 in.) and $0.005R_{\mathrm{i}}$, respectively.

The next set of results is concerned with the effect of material nonlinearity on the post-buckling and post-yield response of the cross-ply [90/0/90] (plane strain) thick ring. Layer material lay-up is given in Table 1, while the material nonlinearity is as shown in Fig. 15(a) and (b), providing nonlinear elastic property corresponding to transverse shear modulus, G_{TT}. Since a fiber-reinforced composite lamina is transversely isotropic, the plane of isotropy being in the plane transverse to the fiber direction, this property is largely matrix dominated. The material nonlinearity pertaining to G_{TT} in graphite/epoxy and other composites, therefore, appears to be nonlinear elastic (hypoelastic), with little residual strain observed. This nonlinearity is described by setting the reference stress, $S_{R_{jj}} = mG_{\mathrm{TT}}$ (see Appendix A for definition), $j = 4$ (no sum on j) for a unidirectional (0°) lamina.

Fig. 16 shows the effect of normalized local imperfection, $w^{**} = w_1/R_{\mathrm{i}}$, on the post-buckling behavior of a thick [90/0/90] composite ring with a fixed modal imperfection ($w_0 = 0.005R_{\mathrm{i}}$) and material nonlinearity ($m = 0.03$, $n = 3.0$). The plots for the corresponding linear elastic material case ($m = \infty$) due to Kim and Chaudhuri (in review) are also shown here (by dashed lines) for the purpose of comparison. Each $p^* = p/p_{\mathrm{cr}}$ vs. $w^* = -w/(R_{\mathrm{i}} - w_0)$ at $\theta = 0°$ plot exhibits a limit point beyond which the equilibrium path is unstable. The curve corresponding to $w_1 = 0$ (and/or $c = 0$) represents nonlocalized solution, and is associated with the periodicity of the classical (modal or harmonic) buckling pattern. It can be clearly seen from these plots

Table 1
Material lay-up definitions of a laminated composite cylindrical shell

Lay-up	E_{xx}	$E_{\theta\theta}$	$E_{\zeta\zeta}$	$G_{x\theta}$	$G_{x\zeta}$	$G_{\theta\zeta}$
$\alpha = 0°$	E_{LL}	E_{TT}	E_{TT}	G_{LT}	G_{LT}	G_{TT}
$\alpha = 90°$	E_{TT}	E_{LL}	E_{TT}	G_{LT}	G_{TT}	G_{LT}

Material data with respect to the global coordinate (x, θ, ζ) for different lay-ups.

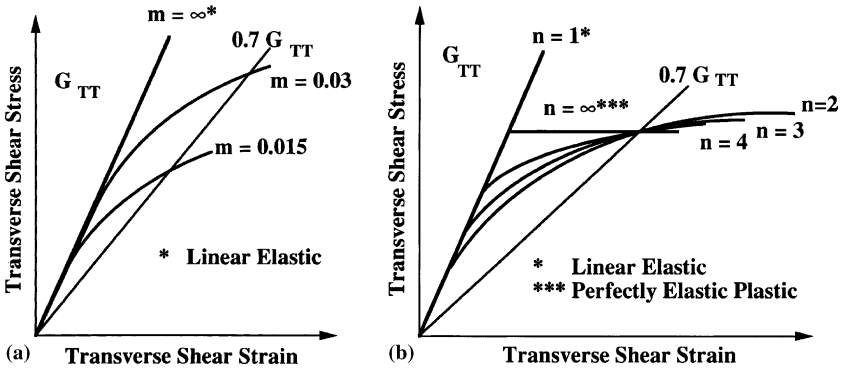

Fig. 15. Nomenclature and property definitions of the nonlinear composite material: (a) G_{TT} curve for different $m = S_R/G_{TT}$) with n fixed and (b) G_{TT} curve for different n with m fixed.

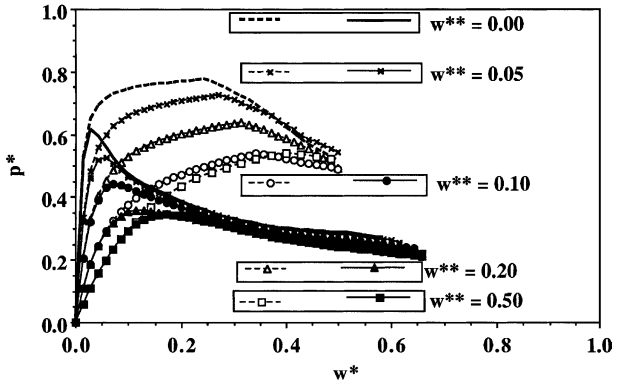

Fig. 16. Effect of local imperfection on the post-buckling behavior of a thick [90/0/90] ring ($R_i/h = 6.0$, $w_0 = 0.005R_i$) nonlinear (—) shear modulus, G_{TT} ($m = 0.03$, $n = 3.0$) and comparison with its linear (- - -) counterpart.

that material nonlinearity has a pronounced effect in lowering the maximum load carrying capacity of the thick composite ring under investigation along with the amplitude of local imperfection. For example, the load carrying capacity reduces down to 51.7% in the case of $w^{**} = 0.005$ compared to the CLT based linearized buckling load of the perfect cylinder. This result qualitatively explains the unacceptably low failure external pressure for thick $(R_i/h = 6)$ $[90_2/0]m$, $m \approx 38$, cylindrical shells in the 83 MPa (12 ksi) range, that has experimentally been observed by Garala (1989), as compared to the computed value of 152 MPa (22 ksi). More quantitatively accurate comparison will require a massive computational effort involving 114 layers, the actual modeling of the entire length of a laminated cylinder with statistically distributed local imperfections of fiber misalignments, resin rich areas, etc. over and above those pertaining to the geometry considered here, which is beyond the scope of the present study.

With the increase of local imperfection amplitude, the limit load (hydrostatic pressure) decreases, and also the limit point appears at an increased normalized deflection (Fig. 16). Additionally, the pressure–deflection curves rise and decay more slowly. These curves tend to flatten to an undetermined lowest pressure level, signaling even more rapid (compared to the linear elastic material case) onset of phase transition in the localized region, and coexistence of two phases, i.e., a highly localized band of shear crippled or kinked phase and its un-shear-crippled (unkinked) counterpart along the circumference of the ring.

Fig. 17(a) exhibits the variation of the normalized radial distance of the deformed inner surface, $R^*(\theta) = R(\theta)/(R_i - w_0)$, measured from the center of the thick cross-ply ring ($R_i/h = 6.0$, $w_0 = 0.005R_i$, $m = 0.03$, $n = 3.0$) during the initial pressurization process with $p^{**} = p/p_{max}$ being in the range of 0–0.3457, which corresponds to the rising branch of the pressure–deflection curve of Fig. 16. Fig. 18(a) exhibits the same variation just before and at the time maximum pressure is reached, i.e., p^{**} being in the range of 0.9102–1.0, which corresponds to the peak of the pressure–deflection curve of Fig. 16, while Fig. 19(a) displays the same for the unphysical falling branch. It is further observed from Fig. 17(b) that the interlaminar shear angle changes drastically from layer to layer through the thickness in a local region ranging from $\theta = 0°$ to $\theta = 9°$ in the initial loading stage, e.g., $p^{**} = p/p_{max} = 0.0977$. This phenomenon suggests that formation of shear-crippling triggered by the combined effect of material nonlinearity and local imperfection at the meso-structural (i.e., lamina) level may be the dominant compressive failure mode for a thick section composite ring, long before the occurrence of global or structural instability failure with an associated periodic buckling pattern. A very low yielding stress or large local imperfection may be expected to lead to this failure mode. As can be seen in Figs. 16, 17(a) and 18(a), the hydrostatic pressure continues

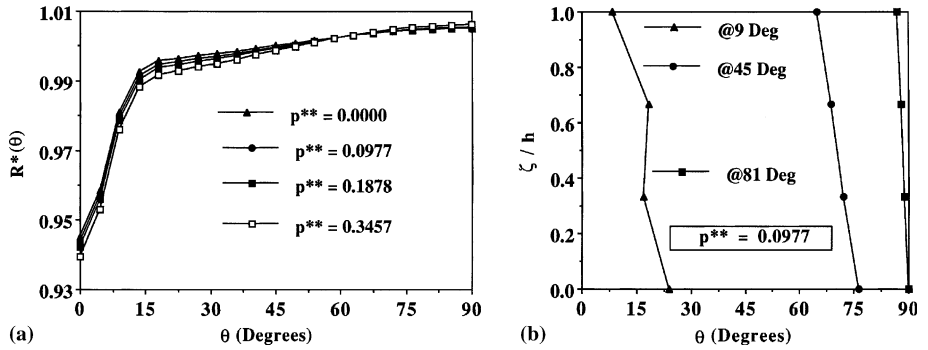

Fig. 17. Displacement patterns (rising pressure) of a thick [90/0/90] ring ($R_i/h = 6.0$, $w_0 = 0.005R_i$) with nonlinear shear modulus, G_{TT} ($m = 0.03$, $n = 3.0$) along the circumferential direction: (a) normalized radial coordinate vs. angle and (b) normalized circumferential displacement at three different angles.

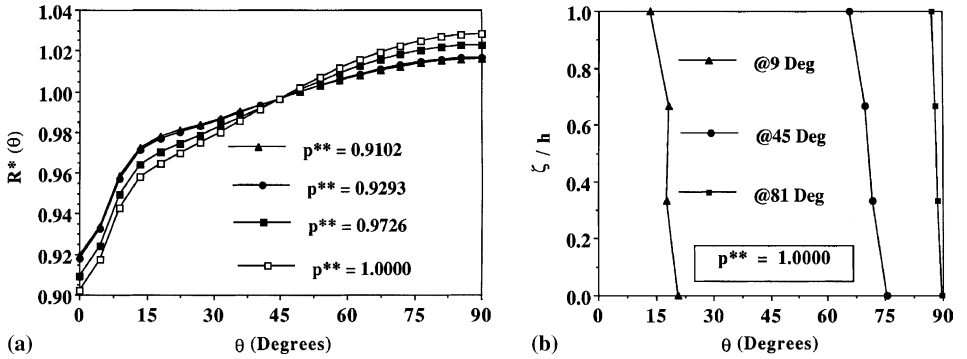

Fig. 18. Displacement patterns (near peak pressure) of a thick [90/0/90] ring ($R_i/h = 6.0$, $w_0 = 0.005R_i$) with nonlinear shear modulus, G_{TT} ($m = 0.03$, $n = 3.0$) along the circumferential direction: (a) normalized radial coordinate vs. angle and (b) normalized circumferential displacement at three different angles.

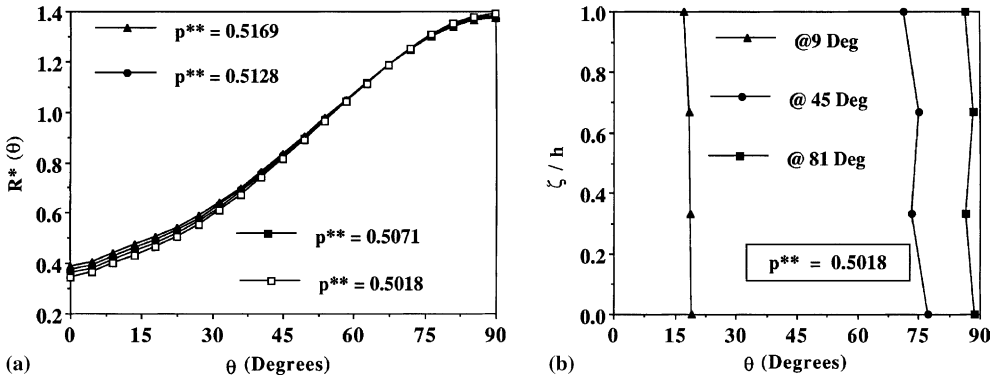

Fig. 19. Displacement patterns (falling pressure) of a thick [90/0/90] ring ($R_i/h = 6.0$, $w_0 = 0.005R_i$) with nonlinear shear modulus, G_{TT} ($m = 0.03$, $n = 3.0$) along the circumferential direction: (a) normalized radial coordinate vs. angle and (b) normalized circumferential displacement at three different angles.

to increase with displacement and reaches the theoretical maximum point (p_{max}). When the pressure reaches its theoretical maximum point, the transverse deflection nodal line shifts to $\theta = 50°$ (approx.), while the layerwise variation of shear angle through thickness that results in shear-crippling pattern of circumferential displacement as well as dimple patterns of transverse deflection tends to delocalize or spread out along the circumferential direction (Fig. 18(a) and (b)). This trend toward delocalization continues well after the limit points (Fig. 19(a) and (b)) in the falling (non-physical) branches of the pressure–deflection curves of Fig. 16.

In this connection, it may be worthwhile to mention that the theoretical limit point pressure, p_{max}, is unattainable, because of the existence of an unstable equilibrium path that follows the limit point, and which, as has been discussed earlier, results from the combined effect of local imperfection and/or material nonlinearity. Consequently, it will switch to a localization mode, which is compatible with meso-structural level deformation mode or pattern, followed by an approach to the onset of phase transition with a significant drop of the load carrying capacity of the composite [90/0/90] ring under investigation. In analogy to phase transition phenomena such as condensation of gases, the melting of solids, phenomena of ferromagnetism and antiferromagnetism, the famous family of lambda-transitions—e.g., order-disorder transitions in alloys, the transition from liquid He I to liquid He II (superfluidity of liquid helium at low temperatures) or the transition from a normal to a superconducting material (superconductivity of metal at low temperatures) and so on (Pathria, 1977) studied in condensed matter physics, this represents a long range order (of nonlocal or gage theories) that is intimately connected with spontaneous symmetry breaking. For example, there is a long range order in the ferromagnet—all the spins are lined up in the same direction, resulting in spontaneous breaking of rotational invariance (Mattuck, 1976; Zee, 1995). In the example problem studied here, localization of the deformation pattern is associated with spontaneous breaking of the periodicity of classical (modal or harmonic) buckling patterns.

A qualitative understanding of the initiation of the shear-crippling (kink band) process can be obtained by considering the relation of applied pressure acting upon a circumferential arc of half-length c, representing a local imperfection region, of a cylindrical section of unit axial length (force) to the deflection as shown in Fig. 16. The qualitative argument for initiation of shear crippling in a thick cross-ply ring (infinitely long cylindrical shell) is similar to that for a number of localization phenomena—necking of a metal bar in tension (Hutchinson and Neale, 1983), shear banding followed by necking in a polycarbonate bar under tension (Lu and Ravi-Chandar, 1999), initiation of bulging in a party balloon (Chater and Hutchinson, 1984), and various kinds of phase transition phenomena mentioned earlier. The shear crippling is a

phenomenon associated with localization of the post-buckling deformation pattern in a manner described by Tvergaard and Needleman (1980, 2000).

In analogy to what is well-known in the phase transition literature, the slope of p^* vs. $w^* = -w/(R_i - w_0)$ curves (Fig. 16), can never be negative. These curves represent iso-thickness-shear states, which are analogous to isotherms of the phase transition literature. While in the absence of any localized or dimple type imperfection, the slope may be expected to be positive until failure, the presence of such defects, representing initial thickness shear strains, can cause a region with near-zero slope to exist, whereby the structure may nearly lose its stiffness. The existence of such a region in the p^* vs. w^* diagram corresponds to the coexistence of two phases, namely a highly localized band (of half-width, c) of shear crippled phase and its un-shear-crippled counterpart in the rest of the ring. In analogy to the phase transition phenomena, the dimple type imperfection may be treated as an impurity or dopant. An understanding analogous to how impurities localize electron states in condensed matter (see Zee, 1995) is helpful for interpretation of the experimentally observed (see Chaudhuri, 1991; Garala, 1989; Garala and Chaudhuri, 1993) localization of shear crippled bands. The aforementioned near-zero slope constitutes a direct evidence of the onset of phase transition in the system.

It is worthwhile to note in this connection that as long as one uses the exact geometry for modeling the initial localized defects represented here by the dimple type imperfection, and exact constitutive relations, such as nonlinear elastic (hypoelastic) behavior of G_{TT} of a unidirectional lamina employed here, the unphysical region of negative slope in the p^* vs. w^* diagram would never appear. The appearance of such an unphysical region in the present case is then a direct consequence of simplifying assumptions, that eliminate the very possibility of the structural system passing through a state or region of flatness in the p^* vs. w^* diagram, in which there coexist two phases of different transverse shear strains. This kind of discrepancy is usually corrected by the Maxwell construction (e.g., equal areas in Fig. 13 of Chaudhuri and Kim, 1997). Introduction of dimple type imperfection and nonlinear G_{TT} in the present analysis has then eliminated the need for employment of such an artifice as the Maxwell construction. This opens the door for the possibility that under favorable conditions, such as the material nonlinearity and presence of severe localized (dimple) type imperfection, which is the archetype of the class of localized defects, such as fiber misalignment defects, resin rich areas etc. (Figs. 3 and 4), the equilibrium configuration of the externally pressurized composite ring will involve a multi-phase—i.e., localized shear crippled (kinked) band and its un-shear-crippled (unkinked) counterpart—state. It is further noteworthy that the observed microstructural ordering of the shear-kinked fibers in a localized shear crippled or kinked band (see Chaudhuri, 1991) is analogous to long range order that arises in the case of collective states of condensed media formed under phase transition of the second kind, such as superfluidity of liquid helium, and the superconductivity and ferromagnetism of metals, which exist only at temperatures below the critical temperature (see Mattuck, 1976; Popov and Yarunin, 1988).

The above localized shear-crippling phenomenon may be called an interaction or meso-structural instability type failure mode that results from a coupling between macro-structural (periodic or modal) and micro-structural (kink band) instabilities, unless the material itself succumbs to the strength failure mode before the occurrence of such interaction type failure mode. It is obviously seen that a three-dimensional or quasi-three-dimensional theory, such as the LLDT is essential in order to capture the meso-structure-related instability failure such as interlaminar shear crippling, triggered by the combined presence of local imperfection and material nonlinearity.

7. Summary and conclusions

A fully nonlinear analysis for prediction of localization representing shear-crippling (kinkband) instability in a thick laminated composite (plane strain) ring (infinitely long cylindrical shell) is presented. The

analysis accounts for both material (hypoelastic behavior) and geometric nonlinearities, the latter incorporating the completely nonlinear strain-displacement relations, in contrast to the commonly used von Karman type nonlinear approximation. The fully nonlinear kinematic relations are employed in the present study so that stable and unstable equilibrium paths in the advanced nonlinear regime can be accurately predicted. The primary accomplishment of the present investigation is prediction of meso(lamina)-structure-related equilibrium paths, which are often unstable in the presence of local imperfections and/or material nonlinearity, and which are considered to "bifurcate" from the primary equilibrium paths, representing periodic buckling patterns pertaining to global or structural level stability of the thick cross-ply ring with modal or harmonic imperfection.

A special purpose nonlinear finite element computer code, referred to as NLSAMP, is developed to predict the afore-mentioned deformation/instability behavior of laminated shell type structures and evaluate failure modes when hydrostatic compressive loads are applied. The present nonlinear finite element solution methodology, based on the total Lagrangian formulation, employs a quasi-three-dimensional hypothesis, known as the LLDT to capture the three-dimensional interlaminar (especially, shear) deformation behavior, associated with the localized interlaminar shear-crippling failure. A curvilinear side layer element with 8 nodes each on the top and bottom surfaces of a layer has been implemented to model the quasi-three-dimensional interlaminar deformation behavior, represented by the LLDT. The most important computational feature of the NLSAMP is successful implementation of an incremental displacement control technique combined with an incremental force control scheme, during the solution process.

A thick laminated composite [90/0/90] imperfect (plane strain) ring is investigated with the objective of analytically studying its premature compressive failure behavior. In order to investigate localization of the buckling pattern, a local or dimple shaped imperfection superimposed on a fixed modal or harmonic one is selected. What follows is a list of useful conclusions drawn from the numerical results:

(i) Numerical results suggest that interlaminar shear/normal deformation (especially, the former) is primarily responsible for appearance of a limit (maximum pressure) point on the post-buckling equilibrium path associated with a periodic (modal or harmonic) buckling pattern, for which a modal imperfection serves as a perturbation. Localization of the buckling pattern results from bifurcation at or near this limit point.

(ii) With the increase of local imperfection amplitude, the limit load (hydrostatic pressure) decreases, and also the limit point appears at an increased normalized deflection.

(iii) Material nonlinearity has a pronounced effect in lowering the maximum load carrying capacity of the thick composite ring under investigation along with the amplitude of local imperfection. The displacement corresponding to maximum pressure is also delayed with the imperfection amplitude as in the linear elastic material case.

(iv) When the pressure reaches its theoretical maximum point, the transverse deflection nodal line shifts to $\theta = 50^\circ$ (approx.), while the layerwise variation of shear angle through thickness that results in shear-crippling pattern of circumferential displacement as well as dimple patterns of transverse deflection tends to delocalize or spread out along the circumferential direction.

(v) The pressure–deflection curves tend to flatten (nearly zero slope) in the presence of material nonlinearity and with the increase of the amplitude of localized (dimple) imperfection, to an undetermined lowest pressure level, signaling the onset of phase transition in the localized region, and coexistence of two phases, i.e., a highly localized band of shear crippled (kinked) phase and its un-shear-crippled (unkinked) counterpart along the circumference of the ring.

(vi) The computed theoretical limit point pressure is unattainable, because of the existence of an unstable equilibrium path that follows the limit point, and which results from the combined effect of local imperfection and/or material nonlinearity. It will switch to a localization mode, which is com-

patible with meso-structural level deformation mode or pattern, followed by an approach to the onset of phase transition with a significant drop of the load carrying capacity of the composite [90/0/90] ring under investigation. In analogy to phase transition phenomena in condensed matter physics, this represents a long range order (of nonlocal or gage theories) that is intimately connected with spontaneous symmetry breaking. In the example problem studied, localization of the deformation pattern is associated with spontaneous breaking of the periodicity of classical or modal buckling patterns.

(vii) Introduction of dimple type imperfection and nonlinear G_{TT} in the present analysis eliminates the need for employment of such an artifice as the Maxwell construction. This opens the door for the possibility that under favorable conditions, such as the material nonlinearity and presence of severe localized (dimple) type imperfection, which is the archetype of the class of localized defects, such as fiber misalignment defects, resin rich areas, etc., the equilibrium configuration of the externally pressurized composite ring will involve a multi-phase—i.e., localized shear crippled (kink) band and its un-shear-crippled (unkinked) counterpart—state.

(viii) The observed micro-structural ordering of the shear-kinked fibers in a localized shear crippled or kinked band is analogous to long range order that arises in the case of collective states of condensed media formed under phase transition of the second kind.

(ix) Onset of the interlaminar shear-crippling (kinkband) type instability, which represents an interaction or meso-structural instability type failure mode that results from a coupling between macro-structural (periodic or modal) and micro-structural (kink band) instabilities, and is triggered by the combined effect of material nonlinearity and local (e.g., dimple) imperfection at the meso-structural (i.e., lamina) level appears to be the dominant compressive failure mode. Structural (periodic) buckling or limit load can be attained, only if the lamina material can survive this meso-structure-related instability failure.

(x) Although the FSDT appears to be adequate for prediction of an accurate load–displacement solution and macrostructural level buckling of a cross-ply cylindrical shell made of a linear elastic material and with modal imperfection, a quasi-three-dimensional theory such as the LLDT is essential to capture the meso-structure-related instability failure such as localized interlaminar shear crippling, triggered by the combined presence of local imperfection and material nonlinearity.

Acknowledgements

Initial phase of this research was performed under the sponsorship of In-house Research Program (IR) at the Carderock Division, NSWC and the Office of Naval Research (ONR) through the Navy Laboratory Participation Program (NLPP), and also a grant to the University of Utah. The authors are grateful for helpful guidance received from the program monitors and collaborating Navy scientists—Dr. Yapa Rajapakse of ONR, and Drs. Bruce Douglas, Joseph Corrado, Martin Krenzke and Himatlal Garala, Carderock Division, NSWC.

Appendix A. Constitutive relations for an orthotropic lamina

Taking into account nonlinear elastic (hypoelastic) behavior (as opposed to plasticity) and neglecting the thermal and hygrothermal effects, the incremental strain-stress relations of the kth orthotropic lamina in terms of the principal material directions (x, β, z) are given as follows:

$$\begin{Bmatrix} {}_0\varepsilon_{xx}^{(k)} \\ {}_0\varepsilon_{\beta\beta}^{(k)} \\ {}_0\varepsilon_{zz}^{(k)} \\ {}_0\varepsilon_{\beta z}^{(k)} \\ {}_0\varepsilon_{xz}^{(k)} \\ {}_0\varepsilon_{x\beta}^{(k)} \end{Bmatrix} = \begin{bmatrix} \Sigma_{11}^{(k)} & \Sigma_{12}^{(k)} & \Sigma_{13}^{(k)} & 0 & 0 & 0 \\ \Sigma_{12}^{(k)} & \Sigma_{22}^{(k)} & \Sigma_{23}^{(k)} & 0 & 0 & 0 \\ \Sigma_{13}^{(k)} & \Sigma_{23}^{(k)} & \Sigma_{33}^{(k)} & 0 & 0 & 0 \\ 0 & 0 & 0 & \Sigma_{44}^{(k)} & 0 & 0 \\ 0 & 0 & 0 & 0 & \Sigma_{55}^{(k)} & 0 \\ 0 & 0 & 0 & 0 & 0 & \Sigma_{66}^{(k)} \end{bmatrix} \begin{Bmatrix} {}_0S_{xx}^{(k)} \\ {}_0S_{\beta\beta}^{(k)} \\ {}_0S_{zz}^{(k)} \\ {}_0S_{\beta z}^{(k)} \\ {}_0S_{xz}^{(k)} \\ {}_0S_{x\beta}^{(k)} \end{Bmatrix}. \tag{A.1}$$

In the above equation, the compliance matrix components Σ_{ij}'s can be approximated analytically by the method of Ramberg and Osgood (1934) who have suggested that rising stress–strain curves with a smooth knee be represented by the relation

$$\Sigma_{jj}^{(k)} = \frac{1}{E_{jj}^{(k)}}\left[1 + \frac{3}{7}\left(\frac{{}_0^tS_{jj}^{(k)}}{S_{Rjj}^{(k)}}\right)^{n-1}\right], \quad j = 1,\ldots,6 \text{ (no sum on } j) \tag{A.2a}$$

and

$$\Sigma_{12}^{(k)} = -\nu_{12}^{(k)}\Sigma_{11}^{(k)}, \quad \Sigma_{13}^{(k)} = -\nu_{13}^{(k)}\Sigma_{11}^{(k)}, \quad \Sigma_{23}^{(k)} = -\nu_{23}^{(k)}\Sigma_{22}^{(k)}, \tag{A.2b}$$

where $E_{jj}^{(k)}$ and ${}_0^tS_{jj}^{(k)}$ denote elastic (Young's or shear) moduli and stress components at time t, respectively, of the kth lamina material, while $\nu_{12}^{(k)}$, $\nu_{13}^{(k)}$ and $\nu_{23}^{(k)}$ represent major Poisson's ratios in the x–β, x–z and β–z planes (surfaces), respectively, of the same. Details of nomenclature and property definitions of the non-linear (hypoelastic) composite material are shown in Fig. 6.

The stress $S_{Rjj}^{(k)}$ is defined as the stress at which $E_{Sjj}^{(k)} = \left(\Sigma_{jj}^{(k)}\right)^{-1} = 0.7E_{jj}^{(k)}$, where $E_{Sjj}^{(k)}$ is the secant modulus. The exponent n, known as the hardening parameter, is found from the expression for the secant modulus thus defined:

$$\frac{E_{jj}^{(k)}}{E_{Sjj}^{(k)}} = 1 + \frac{3}{7}\left(\frac{{}_0^tS_{jj}^{(k)}}{S_{Rjj}^{(k)}}\right)^{n-1}, \tag{A.3a}$$

with

$$S_{Rjj}^{(k)} = mE_{jj}^{(k)}. \tag{A.3b}$$

Evaluation of Eq. (A.3a) at $E_{Sjj}^{(k)} = 0.85E_{jj}^{(k)}$ gives

$$n = \frac{\log_{10}(0.441)}{\log_{10}(S_2^{(k)}/S_{Rjj}^{(k)})} + 1, \tag{A.4}$$

where $S_2^{(k)}$ is the stress at $E_{Sjj}^{(k)} = 0.85E_{jj}^{(k)}$. It may be noted that the linear elastic and the perfectly elastic–plastic cases can be obtained by substituting $S_{Rjj} = \infty$ and $n = \infty$, respectively, into Eq. (A.2). The constitutive relation for each lamina can be obtained by inversion of Eq. (A.1) as follows:

$$\begin{Bmatrix} {}_0S_{xx}^{(k)} \\ {}_0S_{\beta\beta}^{(k)} \\ {}_0S_{zz}^{(k)} \\ {}_0S_{\beta z}^{(k)} \\ {}_0S_{xz}^{(k)} \\ {}_0S_{x\beta}^{(k)} \end{Bmatrix} = \begin{bmatrix} Q_{11}^{(k)} & Q_{12}^{(k)} & Q_{13}^{(k)} & 0 & 0 & 0 \\ Q_{12}^{(k)} & Q_{22}^{(k)} & Q_{23}^{(k)} & 0 & 0 & 0 \\ Q_{13}^{(k)} & Q_{23}^{(k)} & Q_{33}^{(k)} & 0 & 0 & 0 \\ 0 & 0 & 0 & Q_{44}^{(k)} & 0 & 0 \\ 0 & 0 & 0 & 0 & Q_{55}^{(k)} & 0 \\ 0 & 0 & 0 & 0 & 0 & Q_{66}^{(k)} \end{bmatrix} \begin{Bmatrix} {}_0\varepsilon_{xx}^{(k)} \\ {}_0\varepsilon_{\beta\beta}^{(k)} \\ {}_0\varepsilon_{zz}^{(k)} \\ {}_0\varepsilon_{\beta z}^{(k)} \\ {}_0\varepsilon_{xz}^{(k)} \\ {}_0\varepsilon_{x\beta}^{(k)} \end{Bmatrix}. \tag{A.4}$$

$\overline{Q}_{ij}^{(k)}$, $i,j=1,\ldots,6$, the components of the corresponding incremental stiffness matrix of an off-axis lamina, made of a hypoelastic composite material, can be obtained from $Q_{ij}^{(k)}$ via standard transformation rule.

Appendix B. Definition of certain matrix operators

The differential operators, $[B_{\mathrm{LL}}^{(k)}]$, $[B_{\mathrm{NL}}^{(k)}]$ and $[B_{\mathrm{NN}}^{(k)}]$, are as presented below. The matrix $[B_{\mathrm{LL}}^{(k)}]$ referred to in Eqs. (10a), (10b) and (11b) is given as

$$\left[B_{\mathrm{LL}}^{(k)}\right]=\begin{bmatrix} \frac{\partial}{\partial x} & 0 & 0 \\ 0 & \frac{1}{g_\beta^{(k)}}\frac{\partial}{\partial\beta} & \frac{1}{g_\beta^{(k)}} \\ 0 & 0 & \frac{\partial}{\partial z} \\ 0 & \frac{\partial}{\partial z}-\frac{1}{g_\beta^{(k)}} & \frac{1}{g_\beta^{(k)}}\frac{\partial}{\partial\beta} \\ \frac{\partial}{\partial z} & 0 & \frac{\partial}{\partial x} \\ \frac{1}{g_\beta^{(k)}}\frac{\partial}{\partial\beta} & \frac{\partial}{\partial x} & 0 \end{bmatrix}, \tag{B.1}$$

while the matrix $[B_{\mathrm{NL}}^{(k)}]$ referred to in Eqs. (10b) and (11b) is given as follows:

$$\left[B_{\mathrm{NL}}^{(k)}\right]=\begin{bmatrix} R_{11}^{(k)}\frac{\partial}{\partial x} & R_{12}^{(k)}\frac{\partial}{\partial x} & R_{13}^{(k)}\frac{\partial}{\partial x} \\ \frac{R_{21}^{(k)}}{g_\beta^{(k)}}\frac{\partial}{\partial\beta} & \frac{1}{g_\beta^{(k)}}\left(R_{22}^{(k)}\frac{\partial}{\partial\beta}-R_{23}^{(k)}\right) & \frac{1}{g_\beta^{(k)}}\left(R_{23}^{(k)}\frac{\partial}{\partial\beta}+R_{22}^{(k)}\right) \\ R_{31}^{(k)}\frac{\partial}{\partial z} & R_{32}^{(k)}\frac{\partial}{\partial z} & R_{33}^{(k)}\frac{\partial}{\partial z} \\ \frac{R_{31}^{(k)}}{g_\beta^{(k)}}\frac{\partial}{\partial\beta}+R_{21}^{(k)}\frac{\partial}{\partial z} & R_{22}^{(k)}\frac{\partial}{\partial z}+\frac{R_{32}^{(k)}}{g_\beta^{(k)}}\frac{\partial}{\partial\beta}-\frac{R_{33}^{(k)}}{g_\beta^{(k)}} & \frac{R_{32}^{(k)}}{g_\beta^{(k)}}+\frac{R_{33}^{(k)}}{g_\beta^{(k)}}\frac{\partial}{\partial\beta}+R_{23}^{(k)}\frac{\partial}{\partial z} \\ R_{31}^{(k)}\frac{\partial}{\partial x}+R_{11}^{(k)}\frac{\partial}{\partial z} & R_{32}^{(k)}\frac{\partial}{\partial x}+R_{12}^{(k)}\frac{\partial}{\partial z} & R_{33}^{(k)}\frac{\partial}{\partial x}+R_{13}^{(k)}\frac{\partial}{\partial z} \\ \frac{R_{11}^{(k)}}{g_\beta^{(k)}}\frac{\partial}{\partial\beta}+R_{21}^{(k)}\frac{\partial}{\partial x} & R_{22}^{(k)}\frac{\partial}{\partial x}+\frac{R_{12}^{(k)}}{g_\beta^{(k)}}\frac{\partial}{\partial\beta}-\frac{R_{13}^{(k)}}{g_\beta^{(k)}} & R_{23}^{(k)}\frac{\partial}{\partial x}+\frac{R_{13}^{(k)}}{g_\beta^{(k)}}\frac{\partial}{\partial\beta}+\frac{R_{12}^{(k)}}{g_\beta^{(k)}} \end{bmatrix} \tag{B.2}$$

in which

$$\left\{R_{ij}^{(k)}\right\}=\left[B_{\mathrm{NN}}^{(k)}\right]\left\{\bar{\mathbf{v}}^{(k)}\right\}, \tag{B.3}$$

with

$$\left\{R_{ij}^{(k)}\right\}=\left\{R_{11}^{(k)}\quad R_{12}^{(k)}\quad R_{13}^{(k)}\quad R_{21}^{(k)}\quad R_{22}^{(k)}\quad R_{23}^{(k)}\quad R_{31}^{(k)}\quad R_{32}^{(k)}\quad R_{33}^{(k)}\right\}^{\mathrm{T}}, \tag{B.4}$$

$$\left\{\bar{\mathbf{v}}^{(k)}\right\}=\left\{{}_{0}^{t}u^{(k)}\quad {}_{0}^{t}v^{(k)}\quad {}_{0}^{t}w^{(k)}\right\}^{\mathrm{T}}, \tag{B.5}$$

where the components of the vector $\left\{\bar{\mathbf{v}}^{(k)}\right\}$ are known displacements at time t. The matrix $\left[B_{\mathrm{NN}}^{(k)}\right]$ referred to in Eqs. (10b) and (B.3) is given as follows:

$$\left[B_{\mathrm{NN}}^{(k)}\right]=\begin{bmatrix} \frac{\partial}{\partial x} & 0 & 0 & \frac{1}{g_\beta^{(k)}}\frac{\partial}{\partial\beta} & 0 & 0 & \frac{\partial}{\partial z} & 0 & 0 \\ 0 & \frac{\partial}{\partial x} & 0 & 0 & \frac{1}{g_\beta^{(k)}}\frac{\partial}{\partial\beta} & -\frac{1}{g_\beta^{(k)}} & 0 & \frac{\partial}{\partial z} & 0 \\ 0 & 0 & \frac{\partial}{\partial x} & 0 & \frac{1}{g_\beta^{(k)}} & \frac{1}{g_\beta^{(k)}}\frac{\partial}{\partial\beta} & 0 & 0 & \frac{\partial}{\partial z} \end{bmatrix}^{\mathrm{T}}. \tag{B.6}$$

The layerwise linear distribution of displacement matrix, $[T_{\mathrm{BT}}]$, referred to in Eqs. (10) and (11) can be written as follows (see Kim and Chaudhuri, 1995):

$$\left[T_{\mathrm{BT}}^{(k)}(z)\right] = \begin{bmatrix} 1-\frac{z}{h_k} & 0 & 0 & \frac{z}{h_k} & 0 & 0 \\ 0 & 1-\frac{z}{h_k} & 0 & 0 & \frac{z}{h_k} & 0 \\ 0 & 0 & 1-\frac{z}{h_k} & 0 & 0 & \frac{z}{h_k} \end{bmatrix}. \tag{B.7}$$

The quadratic global interpolation function matrix, $[\Phi]$, referred to in Eqs. (10) and (11) is given by

$$[\Phi(r,s)] = \begin{bmatrix} \{\psi\} & \{0\} & \{0\} & \{0\} & \{0\} & \{0\} \\ \{0\} & \{\psi\} & \{0\} & \{0\} & \{0\} & \{0\} \\ \{0\} & \{0\} & \{\psi\} & \{0\} & \{0\} & \{0\} \\ \{0\} & \{0\} & \{0\} & \{\psi\} & \{0\} & \{0\} \\ \{0\} & \{0\} & \{0\} & \{0\} & \{\psi\} & \{0\} \\ \{0\} & \{0\} & \{0\} & \{0\} & \{0\} & \{\psi\} \end{bmatrix}, \tag{B.8}$$

wherein

$$\{\psi\} = \{\,\psi_1 \quad \psi_2 \quad \psi_3 \quad \psi_4 \quad \psi_5 \quad \psi_6 \quad \psi_7 \quad \psi_8\,\} \tag{B.9}$$

and $\{0\}$ is 1×8 null matrix. $\psi_k(r,s)$, $k = 1,\ldots,8$, are the shape functions as used for displacements and coordinates.

Finally, the stress matrix, $[{}^t_0\widehat{S}_{ij}]$, and stress vector, $\{{}^t_0\overline{S}_{ij}\}$, referred to in Eqs. (10b) and (11b), respectively, are given as follows:

$$[{}^t_0\widehat{S}_{ij}] = \begin{bmatrix} [{}^t_0S^*] & [0] & [0] \\ [0] & [{}^t_0S^*] & [0] \\ [0] & [0] & [{}^t_0S^*] \end{bmatrix}, \tag{B.10}$$

with

$$[{}^t_0S^*] = \begin{bmatrix} [{}^t_0S_{11}] & [{}^t_0S_{12}] & [{}^t_0S_{13}] \\ [{}^t_0S_{12}] & [{}^t_0S_{22}] & [{}^t_0S_{23}] \\ [{}^t_0S_{13}] & [{}^t_0S_{23}] & [{}^t_0S_{33}] \end{bmatrix} \tag{B.11}$$

and

$$\{{}^t_0\overline{S}_{ij}\}^{\mathrm{T}} = \{\,{}^t_0S_{11} \quad {}^t_0S_{22} \quad {}^t_0S_{33} \quad {}^t_0S_{23} \quad {}^t_0S_{13} \quad {}^t_0S_{12}\,\}. \tag{B.12}$$

Appendix C. Incremental displacement control technique

In the event of a displacement increment, ${}_0V_q$, being specified at a load step, t to $t+\Delta t$, instead of varying the load parameter, the qth component of the total displacement vector at the first iteration of the time step t to $t+\Delta t$, is incremented by ${}_0V_q$, while the initial solution vector ${}^{t+\Delta t}\{V\}^{(0)}$ is redefined as

$${}^{t+\Delta t}\{\mathbf{V}\}^{(0)} = {}^t\{\mathbf{V}\}, \tag{C.1a}$$

$${}^{t+\Delta t}\lambda^{(0)} = {}^t\lambda, \tag{C.1b}$$

where the qth component of the total displacement at time $t+\Delta t$, ${}^{t+\Delta t}V_q^{(0)} = {}^tV_q + {}_0V_q$, while the scalar quantity ${}^{t+\Delta t}\lambda^{(0)}$ represents the initial load level that is calculated at the previous time step. The Newton–Raphson method introduced in calculating prebuckling solution is employed to obtain the unknown incremental displacement vector and the corresponding force vector with ${}_0V_q$ considered as fixed during an iteration. The modified algorithm (see e.g., Batoz and Dhatt, 1979) for solving Eq. (9) then becomes

$$([K_{\mathrm{L}}] + {}^t[K_{\mathrm{N}}])^{(i)}\{{}_0\mathbf{R}\}^{(i)} = {}^{t+\Delta t}\{\mathbf{f}_{\mathrm{N}}\}^{(i-1)}, \tag{C.2a}$$

$$([K_L] + {}^{t}[K_N])^{(i)}\{{}_0\mathbf{Q}\}^{(i)} = {}^{t+\Delta t}\{\mathbf{f}_L\}, \tag{C.2b}$$

where ${}^{t+\Delta t}\{\mathbf{f}_N\}^{(i-1)}$ is the residual vector (i.e., nonlinear force vector) evaluated at the $(i-1)$th iteration of the time step, t to $t+\Delta t$, while ${}^{t+\Delta t}\{\mathbf{f}_L\}$ is the applied load vector that is assumed to be proportional for each time step, which is multiplied by ${}_0\lambda^{(i)}$ to obtain the actual load corresponding to the prescribed displacement. The quantities $\{{}_0\mathbf{R}\}^{(i)}$ and $\{{}_0\mathbf{Q}\}^{(i)}$ are incremental displacements due to the residual force vector and the applied load vector respectively. The complete solution of Eq. (14) is now defined by

$${}^{t+\Delta t}\{\mathbf{V}\}^{(i)} = {}^{t+\Delta t}\{\mathbf{V}\}^{(i-1)} + \{{}_0\mathbf{V}\}^{(i)}, \tag{C.3a}$$

$$\{{}_0\mathbf{V}\}^{(i)} = \{{}_0\mathbf{R}\}^{(i)} + {}_0\lambda^{(i)}\{{}_0\mathbf{Q}\}^{(i)}. \tag{C.3b}$$

The value of incremental load scale factor, ${}_0\lambda^{(i)}$ can be obtained as follows, reflecting that the qth component of the incremental displacement (i.e., ${}_0V_q^{(i)}$) is set to zero during iteration:

$${}_0\lambda^{(i)} = -\frac{{}_0R_q^{(i)}}{{}_0Q_q^{(i)}}, \tag{C.4}$$

where $R_q^{(i)}$ and $Q_q^{(i)}$ are the qth components of vector $\{{}_0\mathbf{R}\}^{(i)}$ and $\{{}_0\mathbf{Q}\}^{(i)}$, respectively. In the present investigation, the total stiffness matrix in Eq. (C.2) is not calculated at each iteration but calculated and factorized at each time step. It is implicitly assumed that the total stiffness matrix remains non-singular at any solution level. Theoretically, if a certain displacement solution corresponds to a critical or singular point, the total stiffness matrix will be singular. However, in practice, it is nearly impossible to obtain a solution vector exactly corresponding to a singular point, due to a large number of components of ${}^{t+\Delta t}\{\mathbf{V}\}^{(i)}$ and possible round-off errors. The above-mentioned algorithm for solving Eq. (C.2) is, therefore, utilized in this investigation without the problem of singularity of the total stiffness matrix encountered. In a situation where the matrix is singular, the previous algorithm should be modified to avoid the singularity in a manner suggested by Zienkiewicz (1971) and Thomas and Gallagher (1975). Furthermore, neither the stiffness matrix need to be reorganized into partitioned form nor the sky-line and bandwidth of the stiffness matrix should be destroyed in the present investigation. Only two different load vectors (i.e., ${}^{t+\Delta t}\{\mathbf{f}_N\}^{(i-1)}$ and ${}^{t+\Delta t}\{\mathbf{f}_L\}$ in Eq. (C.2) are involved, which are back-substituted in the subroutine COLSOL to calculate the incremental displacements simultaneously.

References

Abdallah, M.G., Gascoigne, H.E., Cairnes, D.S., Patton, K.B., 1990. Measurement of deformation in thick composite rings subjected to external pressure. presented at SEM's Spring Conference on Experimental Mechanics and Manufacturer's Exhibit, Albuquerque, NM.

Abdelmoula, R., Damil, N., Poiter-Ferry, M., 1992. Influence of distributed and localized imperfections on the buckling of cylindrical shells under external pressure. Int. J. Solids Struct. 29, 1–25.

Batoz, J.L., Dhatt, G.S., 1979. Incremental displacement algorithms for nonlinear problems. Int. J. Numer. Meth. Engng. 15, 1262–1267.

Chater, E., Hutchinson, J.W., 1984. On the propagation of bulges and buckles. ASME J. Appl. Mech. 51, 269–277.

Chaudhuri, R.A., 1991. Prediction of the compressive strength of thick-section advanced composite laminates. J. Compos. Mater. 25, 1244–1276.

Chaudhuri, R.A., Kim, D.J., 1997. On propagation of shear crippling (Kink band) instability in a long thick laminated composite imperfect cylindrical shell under external pressure. Int. J. Solids Struct. 34, 3455–3486.

Chaudhuri, R.A., Hsia, R.L., 1998. Effect of thickness on the large elastic deformation behavior of laminated shells. Compos. Struct. 43, 117–128.

Chaudhuri, R.A., Hsia, R.L., 1999. Effect of thickness on the large deflection behavior of shells. AIAA J. 37, 403–405.

Chaudhuri, R.A., Xie, M.S., Garala, H.J., 1996. Stress singularity due to kink band weakening a unidirectional composite under compression. J. Compos. Mater. 30, 672–691.

Couch, W.P., Ward, G.D., Blumenberg, W.F., 1969. Investigation of filament-reinforced plastic deep submergence pressure hulls—July, 1966 to March 1969, Department of the Navy, Naval Ship Research and Development Center, Washington, DC, 20007.

Garala, H.J., 1989. Structural evaluation of 8-inch diameter graphite-epoxy composite cylinders subjected to external hydrostatic compressive loading. DTRC Report 89/016.

Garala, H.J., Chaudhuri, R.A., 1993. Structural evaluation of advanced composite thick-section cylinders under biaxial compression. In: Rajapakse, Y. (Ed.), Mechanics of Thick Composites, AMD-vol. 162, pp. 227–236.

Hsia, R.L., Chaudhuri, R.A., 1996. Geometrically nonlinear analysis of a cylindrical shell using surface-parallel quadratic elements. Comput. Struct. 61, 1143–1154.

Hutchinson, J.W., Neale, K.W., 1983. Neck propagation. J. Mech. Phys. Solids 31, 405–426.

Jamal, M., Midani, M., Damil, N., Potier-Ferry, M., 1999. Influence of localized imperfections on the buckling of cylindrical shells under axial compression. Int. J. Solids Struct. 36, 441–464.

Jones, R.M., 1998. Mechanics of Composite Materials, 2nd ed. Taylor and Francis, Philadelphia, PA.

Kim, D.J., Chaudhuri, R.A., in review. Influence of localized imperfection on the instability of isotropic/cross-ply cylindrical shells/rings under hydrostatic pressure. Compos. Struct.

Kim, D.J., Chaudhuri, R.A., 1995. Full and von Karman geometrically nonlinear analyses of laminated cylindrical panels. AIAA J. 33, 2173–2181.

Koiter, W.T., 1945. In: Paris, H.J. (Ed.), The Stability of Elastic Equilibrium (in Dutch). Ph.D. Thesis, Delft, Netherlands, Amsterdam.

Lu, J., Ravi-Chandar, K., 1999. Inelastic deformation and localization in polycarbonate under tension. Int. J. Solids Struct. 36, 391–425.

Mattuck, R.D., 1976. A Guide to Feynman Diagrams in the Many-Body Problem, 2nd ed. McGraw-Hill, New York.

Pathria, R.K., 1977. Statistical Mechanics. Pergamon, Oxford.

Popov, V.N., Yarunin, V.S., 1988. Collective States in Quantum Statistics of Radiation and Matter. Kluwer Academic Publishers, Dordrecht, The Netherlands.

Ramberg, W., Osgood, W.R., 1934. Description of Stress Strain Curves by Three Parameters. NACA-TN 902.

Starnes, J., Williams, J.G., 1982. Failure characteristics of graphite-epoxy structural components loaded in compression. NASA TM 84552.

Thomas, G., Gallagher, R.H., 1975. A Triangular Thin Shell Finite Element: Nonlinear Analysis. NASA CR-2483, Washington, DC.

Tvergaard, V., 1999. Studies of elastic–plastic instabilities. ASME J. Appl. Mech. 66, 3–9.

Tvergaard, V., Needleman, A., 1980. On the localization of buckling patterns. ASME J. Appl. Mech. 47, 613–619.

Tvergaard, V., Needleman, A., 2000. Buckling localization in a cylindrical panel under axial compression. W.T. Koiter Commemorative Issue. Int. J. Solids Struct. 37, 6825–6842.

Waas, A.M., Babcock, C.D., Knauss, W.G., 1990. An experimental study of compression failure of fibrous laminated composites in the presence of stress gradients. Int. J. Solids Struct. 26, 1071–1098.

Xie, W.-C., 2000. Chaos, Soliton and Fractals. Special issue dedicated to localization phenomena in physical and engineering sciences.

Zee, A., 1995. Quantum hall fluids. In: Geyer, H.B. (Ed.), Field Theory, Topology and Condensed Matter Physics. Springer, Berlin, pp. 99–153.

Zienkiewicz, O.C., 1971. Incremental displacement in nonlinear analysis. Int. J. Numer. Meth. Engng. 3, 587–592.